# Mesoscale Convective Vortices Observed during BAMEX. Part II: Influences on Secondary Deep Convection

STANLEY B. TRIER AND CHRISTOPHER A. DAVIS

*National Center for Atmospheric Research,* Boulder, Colorado*

(Manuscript received 13 March 2006, in final form 19 September 2006)

ABSTRACT

Observations from the Bow Echo and Mesoscale Convective Vortex (MCV) Experiment are used to examine the role of the five mesoscale convective vortices described in Part I on heavy precipitation during the daytime heating cycle. Persistent widespread stratiform rain without deep convection occurs for two strong MCVs in conditionally stable environments with strong vertical shear. Two other MCVs in moderate-to-strong vertical shear have localized redevelopment of deep convection (termed secondary convection) on their downshear side, where conditional instability exists. The strongest of the five MCVs occurs in weak vertical shear and has widespread secondary convection, which is most intense on its conditionally unstable southeast periphery. The two MCVs with only localized secondary convection have well-defined mesoscale vertical motion couplets with downshear ascent and upshear descent above the planetary boundary layer (PBL). Although the amplitude is significantly greater, the kinematically derived vertical motion dipole resembles that implied by steady, vortex-relative isentropic flow, consistent with previous idealized (dry) simulations and diagnoses based on operational model analyses. In the other three cases with either widespread precipitation or weak environmental vertical shear, the kinematic and isentropic vertical motion patterns are poorly correlated. Vertical motions above the PBL provide a focus for secondary convection through adiabatic cooling downshear and adiabatic warming upshear of the MCV center. The MCVs occur within surface frontal zones with large temperature and moisture gradients across the environmental vertical shear vector (Part I). Thus, the effect of vertical motions on conditional instability is reinforced by horizontal advections of high equivalent potential temperature air downshear, and low equivalent potential temperature air upshear within the PBL. On average, the quadrant immediately right of downshear (typically southeast of the MCV center) best supports deep convection because of the juxtaposition of greatest mesoscale ascent, high equivalent potential temperature PBL air, and MCV-induced enhancement of the vertical shear.

## 1. Introduction

Davis and Trier (2007, hereafter Part I) document the mature-stage relative vorticity and thermodynamic structure of five long-lived mesoscale convective vortices (MCVs) observed during the Bow Echo and MCV Experiment (BAMEX). These MCVs are each first detected within the stratiform precipitation area of large, nocturnal mesoscale convective systems (MCSs) (Part I, their Fig. 3). In the current study we examine the role of these MCVs in either sustaining or helping to initiate heavy precipitation the following day.

Sustenance or redevelopment of deep convection within MCVs have been illustrated in numerous previous studies (e.g., Johnston 1981; Bosart and Sanders 1981; Menard and Fritsch 1989; Bartels and Maddox 1991; Fritsch et al. 1994; Trier et al. 2000a; Davis et al. 2002; Trier and Davis 2002). Convection that redevelops after the decay of the antecedent MCS, which we refer to as secondary convection (e.g., Carbone et al. 1990), often requires daytime heating or enhanced moisture becoming available in the vicinity of the remnant MCV.

Raymond and Jiang (1990) idealized MCVs as balanced midtropospheric potential vorticity (PV) anomalies and postulated that the lifting associated with PV

* The National Center for Atmospheric Research is sponsored by the National Science Foundation.

*Corresponding author address:* Stanley B. Trier, National Center for Atmospheric Research, P.O. Box 3000, Boulder, CO 80307-3000.
E-mail: trier@ucar.edu

DOI: 10.1175/MWR3399.1

© 2007 American Meteorological Society

anomalies in vertical shear may explain some cases of MCS longevity. Such lifting may also influence the development of secondary convection. In Part I, the diagnosis using a nonlinear balance equation confirms the similar vertical structure of balanced and observed MCV virtual temperature profiles.

The isentropic vertical motion pattern associated with a steady, balanced vortex in environmental vertical shear summarized by Raymond and Jiang (1990) consists of lower-tropospheric ascent downshear and descent upshear of the PV anomaly as the vortex-relative environmental flow moves along the isentropic surfaces of the anomaly (Fig. 1a). An additional reinforcing source of vertical motion results from the vortex tangential flow moving along the isentropic surfaces of the environmental baroclinity (Fig. 1b) within which the vortex is embedded. Raymond and Jiang (1990) found, using a nonlinear balance model, that vertical motions induced by this mechanism were only on the order of several cm $s^{-1}$ ($\mu$b $s^{-1}$). However, they noted that even as the PV anomaly became differentially advected by the environmental vertical shear, ascent (descent) persisted on its downshear (upshear) side, leading to potentially significant maximum vertical displacements of ~500 m within a diurnal cycle.

Trier et al. (2000b) demonstrated the ability of simulated vortices initialized in gradient and thermal wind balance to destabilize idealized thermodynamic environments representative of a composite of observed MCVs (Trier et al. 2000a). Using operational model analyses, Trier and Davis (2002) further showed that MCV-induced balanced ascent helped produce heavy precipitation by contributing substantially to the adiabatic cooling and eventual saturation of air parcels that originated near the top of the planetary boundary layer (PBL). In other cases, MCV-induced vertical motions and horizontal advections may simply provide a focus for deep convection, which is directly initiated by other mechanisms.

Latent heat release in MCVs contributes to vortex stretching, which may promote their persistence in the presence of deformation and differential advection (e.g., Raymond and Jiang 1990; Fritsch et al. 1994; Rogers and Fritsch 2001; Davis and Trier 2002). However, such diabatic heating alters the potential temperature and relative vorticity patterns within the MCV as deep convection redevelops. The possible influences of the diabatic heating on the previously discussed balanced lifting mechanism are not well understood. Moist simulations nonetheless suggest that mesoscale low–midtropospheric ascent, though significantly increased, remains maximized downshear of the vortex center for at least some time ($T \sim 12$ h) after the onset of parameterized convection in idealized vortices resembling MCVs (e.g., Jiang and Raymond 1995) and incipient tropical cyclones (e.g., Frank and Ritchie 1999).

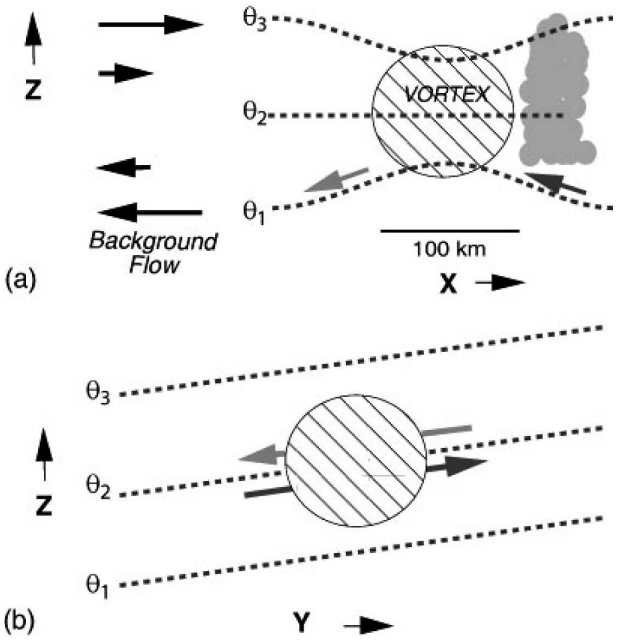


FIG. 1. Schematic of balanced lifting in the vicinity of a positive PV anomaly (hatched) in ambient vertical shear. The vertical motion is associated with (a) the background vertical shear along isentropic surfaces of the vortex and (b) the vortex-induced tangential flow along the isentropic surfaces of the background baroclinic zone. Reproduced from Trier et al. (2000a) and based on Fig. 2 of Raymond and Jiang (1990).

Direct observations of vertical motions within MCVs are scarce, and those published (e.g., Brandes 1990; Jorgensen and Smull 1993; Knievel and Johnson 2002) consist primarily of spatial averages over the entire MCV during the mature-to-dissipating stages of its antecedent MCS. Of potentially greater relevance to forecasting secondary convection are the mesoscale vertical motions within different regions of the remnant MCV circulation during the following heating cycle.

In this paper we diagnose lower-tropospheric mesoscale vertical motions when precipitation within the MCV circulation is either continuing or redeveloping as secondary deep convection. Because of the relatively short ~3-h periods during which the Lear jet deployed dropsondes in BAMEX cases, we are unable to analyze the evolution of these vertical motions, which constitutes a limitation of our study. However, the copious wind and thermodynamic data acquired during these sampling periods (e.g., Davis et al. 2004) combined with National Oceanic and Atmospheric Administration (NOAA) Profiler Network (NPN) wind observations

allow us to analyze, in unprecedented detail, the mesoscale spatial structure of vertical motions and additional aspects of the MCV circulation that influence the convection.

In section 2 we provide an overview of the evolution of MCV precipitation during its second diurnal cycle, including the development of secondary convection, which occurs in three of the five cases. Our data analysis procedures are described in section 3. In section 4 we illustrate how mesoscale vertical motion varies across the MCVs. Here, we also examine the extent to which the full (i.e., kinematically derived) mesoscale vertical motion can be explained by that which arises solely from steady, isentropic processes (Fig. 1) for the five individual BAMEX cases in which MCV strength, the environmental vertical shear, and the distribution of precipitation vary substantially. How the mesoscale vertical motions and other MCV-induced physical processes conspire to help pinpoint regional differences in secondary convection is discussed in section 5.

## 2. Overview of MCV-related precipitation

MCVs persist the day after their nocturnal origination in each of the five Intensive Observing Periods (IOPs). Here we briefly summarize the precipitation associated with the MCVs during the heating cycle following their formation. The environmental vertical shear has a westerly component in all cases (Part I, their Fig. 8) and precipitation is most prevalent downshear (east) of the MCV center. The five IOPs can be divided into three broad categories of the precipitation structure and life cycle. These categories include 1) continuous widespread post-MCS stratiform precipitation with no significant secondary convection (IOPs 1 and 4), 2) nearly complete dissipation of remnant MCS precipitation prior to the redevelopment of afternoon secondary convection downshear of the MCV center (IOPs 5 and 15), and 3) rapid (midmorning) redevelopment of banded secondary convection in multiple locations of the MCV, which is most intense along its east-southeast periphery (IOP 8).

In IOP 1, the midafternoon precipitation is primarily stratiform with weakly convective spiral banded features (Fig. 2a) similar to those previously observed in remnant vortical stratiform regions of dissipating MCSs (e.g., Leary and Rappaport 1987). The well-organized stratiform precipitation moves eastward with the vortex (Fig. 2b) but loses organization by midevening (Fig. 2c). By then, small, scattered storms occur along the southwest margin of the dissipating MCV (Fig. 2c) but this is well after the 1950–2234 UTC data collection.

IOP 4 is a "hybrid" case where the MCV is embedded within a synoptic trough/frontal system (Part I) and thus has the most widespread stratiform precipitation of all cases. This precipitation occurs predominately downshear (east) of the MCV center (Fig. 3). Secondary convection does not occur in this case.

In IOP 5, mid–late-afternoon secondary convection initiates downshear of the MCV center first as a north–south-oriented line (Fig. 4a) and later as an east–west-oriented line (Figs. 4b,c). Both of these features are short lived (<3 h) and do not evolve upscale into an MCS.

Secondary convection in IOP 15 is also confined to downshear but is more extensive than in IOP 5. The first secondary convection appears by early afternoon (Fig. 5a) and develops into a small MCS by mid–late afternoon (Fig. 5b). Slightly after the onset of secondary convection in the vicinity of the MCV, a northeast–southwest-oriented band of convection apparently forced by convergence along a stationary front (not shown) develops over Missouri. These two features eventually merge (Fig. 5b). Despite having localized regions of intense convection, the MCS as a whole never becomes highly organized and dissipates by midevening. The redevelopment of nocturnal convection occurs on the southern flank of the remnant MCV circulation (Fig. 5c) well after the 1920–2207 UTC data collection ceases.

In IOP 8, which is the longest-lived and most intense vortex, secondary convection begins by mid–late morning as small north–south-oriented bands on the east-southeast periphery of the MCV (Fig. 6a). These intense convective bands successively redevelop during the afternoon, increase in length, and individually accelerate eastward faster than the MCV itself (Fig. 6b). Meanwhile, stratiform precipitation with embedded weak convection persists on the western edge and near the MCV center (Fig. 6b). By midevening the convective bands on the east-southeast edge of the MCV no longer develop and the primary region of heavy precipitation is located near the MCV center and to its north (Fig. 6c).

## 3. Analysis methods

In this section we discuss methods used to estimate vertical velocity and other environmental parameters that influence convection initiation within the MCV circulation. Vertical velocity is diagnosed both directly using the kinematic method and also by considering its component implied by steady, isentropic, vortex-relative horizontal motion (Fig. 1).

Kinematic pressure vertical velocity, $\omega \equiv Dp/Dt \sim -\rho g w$, is obtained using mass conservation,

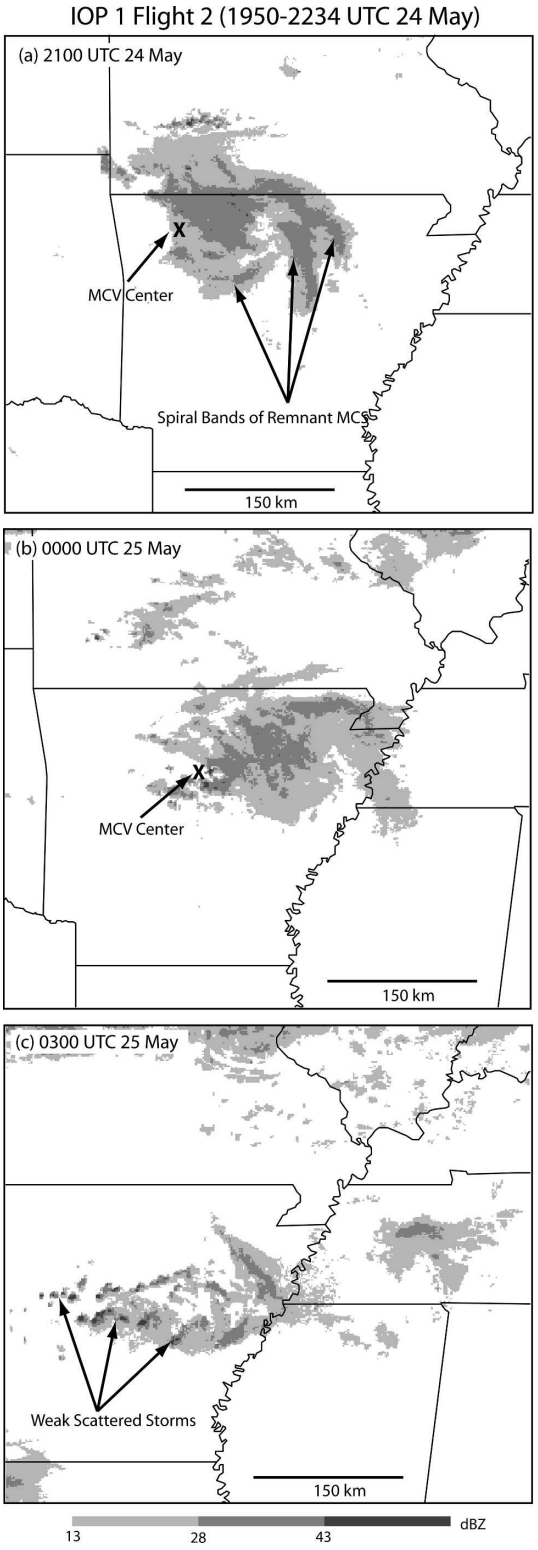


FIG. 2. Composite radar reflectivity in the vicinity of the MCV circulation for the IOP 1 case. The time interval of the dropsonde data collection listed in the title represents the approximate time interval to which the analyses in sections 4 and 5 pertain: (a) 2100 UTC 24 May, (b) 0000 UTC 25 May, and (c) 0300 UTC 25 May.

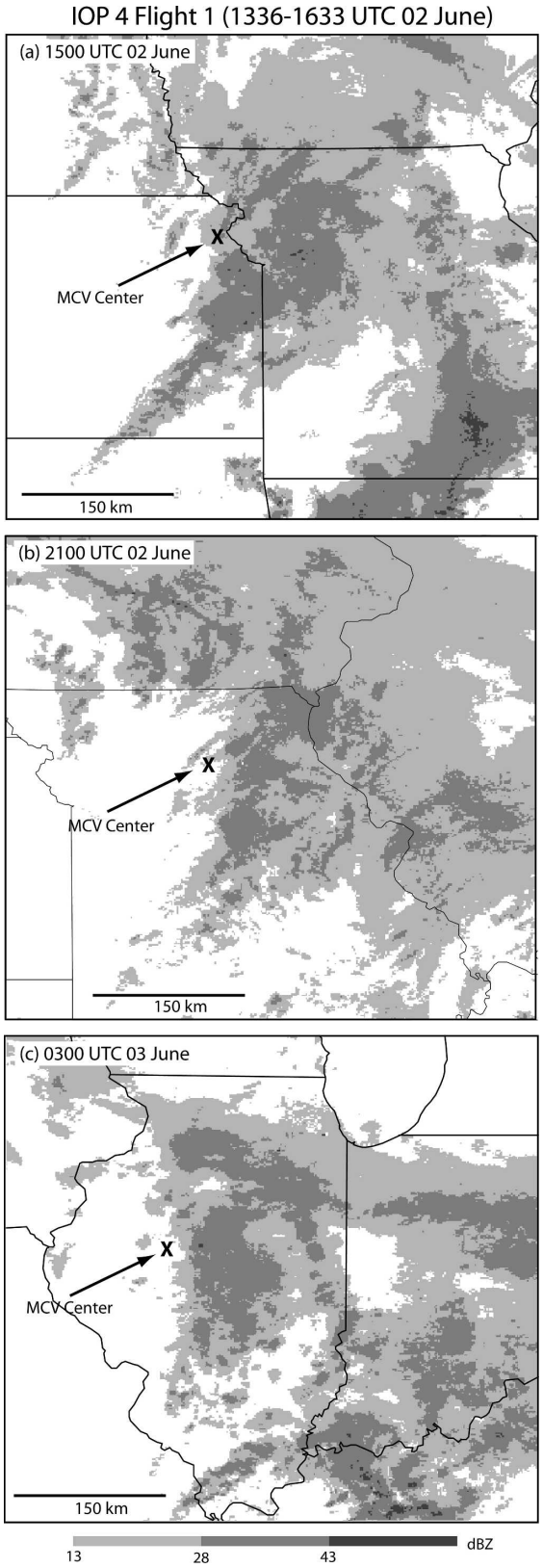


FIG. 3. As in Fig. 2 but for IOP 4: (a) 1500 UTC 2 Jun, (b) 2100 UTC 2 Jun, and (c) 0300 UTC 3 Jun.

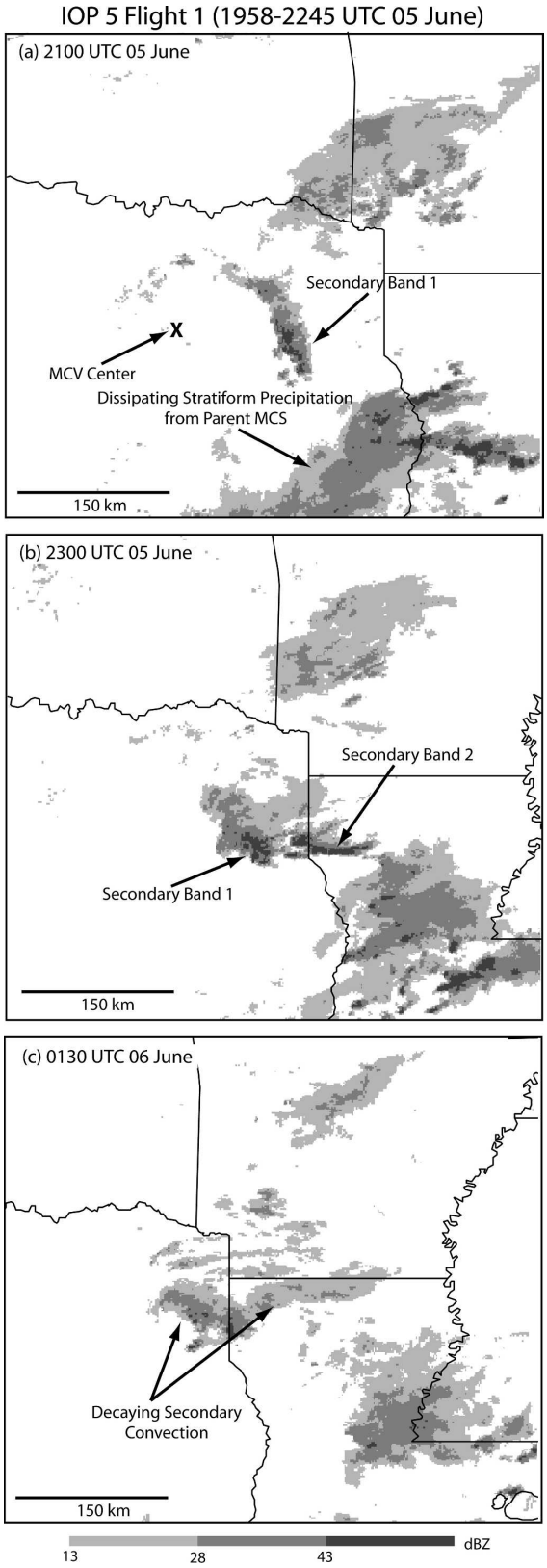


FIG. 4. As in Fig. 2 but for IOP 5: (a) 2100 UTC 5 Jun, (b) 2300 UTC 5 Jun, and (c) 0130 UTC 6 Jun.

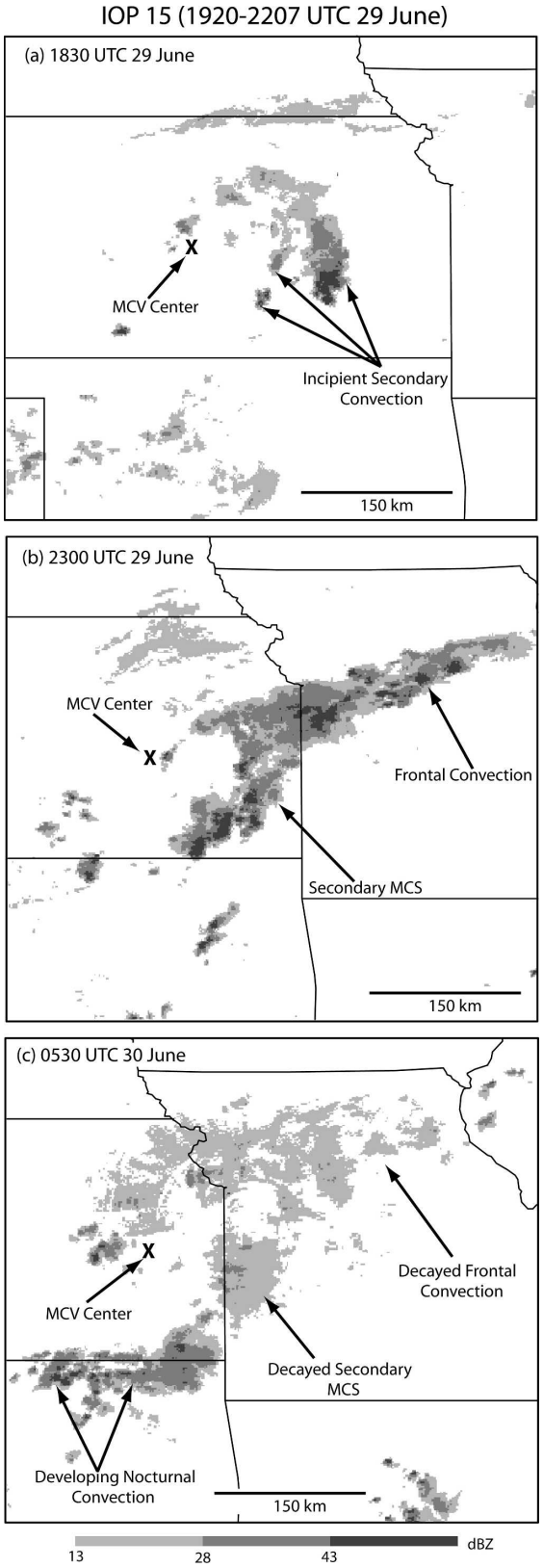


FIG. 5. As in Fig. 2 but for IOP 15: (a) 1830 UTC 29 Jun, (b) 2300 UTC 29 Jun, and (c) 0530 UTC 30 Jun.

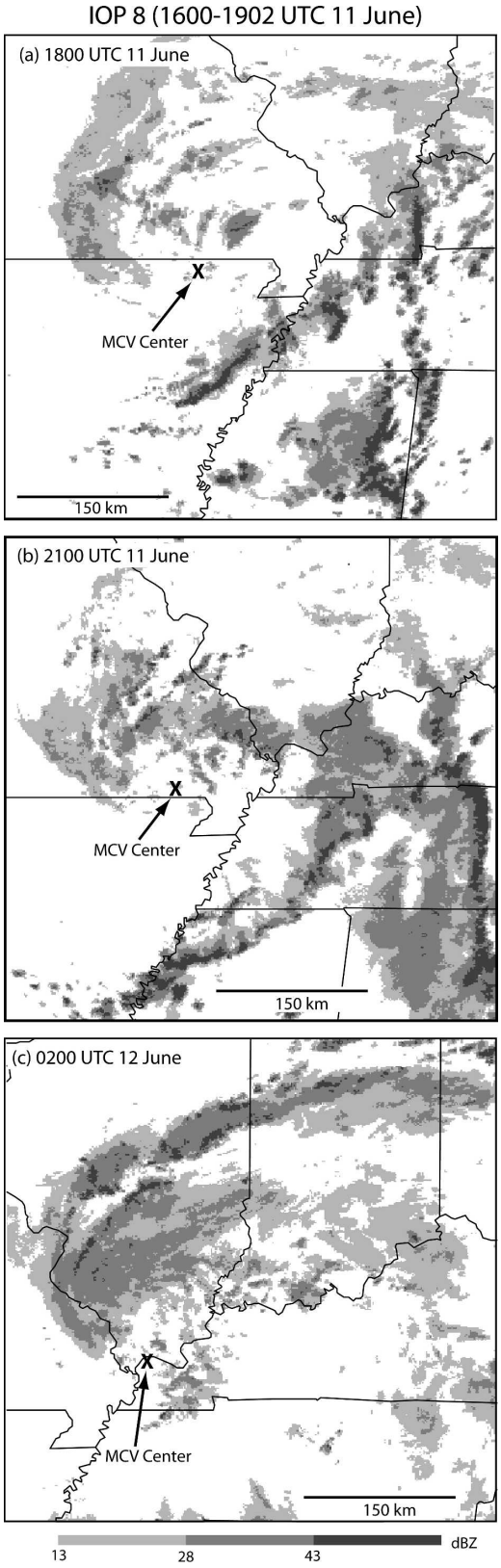


FIG. 6. As in Fig. 2 but for IOP 8: (a) 1800 UTC 11 Jun, (b) 2100 UTC 11 Jun, and (c) 0200 UTC 12 Jun.

$$\omega(p) = -\int_{p(z=0)}^{p(z)} \nabla_p \cdot \mathbf{V}\, dp. \tag{1}$$

The vertical motion due to the typically negligible terrain slope is ignored, resulting in a lower boundary condition of $\omega = 0$. Since we only consider vertical motions from the surface to 600 hPa, no attempt is made to variationally adjust the vertical profiles of $\omega$ and horizontal divergence, $\nabla_p \cdot \mathbf{V}$, such that zero net horizontal divergence occurs in the vertical column (e.g., O'Brien 1970).

The horizontal divergence in (1) is approximated using Bellamy (1949) triangles, which were used to calculate the vertical component of relative vorticity, $\zeta$, in Part I. Assuming the linear variation of winds along triangle legs, the Bellamy calculation of horizontal divergence,

$$\nabla_p \cdot \mathbf{V} = \frac{1}{A}\frac{DA}{Dt}, \tag{2}$$

where the right side of (2) is the fractional change in the triangle area resulting from different wind velocities at the triangle vertices, is equivalent to the line integral method,

$$\nabla_p \cdot \mathbf{V} = \frac{1}{A}\int_c (u\, dy - v\, dx),$$

in which the integration is performed along the three legs of the triangle when $\Delta t \to 0$ (see Davies-Jones 1993 for a more complete discussion). Spencer and Doswell (2001) argue that line integral (triangle) techniques provide substantial improvements in estimating the pattern of spatial derivatives over traditional methods where the derivatives are estimated by finite differencing a gridded field constructed from the original (unequally spaced) observations.

Horizontal divergence is valid at the centroids of triangles composed of observations from the time–space-corrected dataset (Part I), which includes dropsonde, research mobile GPS-Loran Atmospheric Sounding Systems (MGLASS) and operational National Weather Service (NWS) rawinsondes, and NPN wind profiler observations interpolated to 10-hPa increments at each horizontal location. An examination of dropsonde and rawinsonde data indicates that horizontal displacements of these measurements from the surface to 600 hPa rarely exceed 10 km. Errors in $\omega$ due to this limited horizontal drift are not corrected since they are likely small.

The integration of (1) for each triangle begins at the lowest interpolated bottom pressure of the three tri-

angle stations (vertices). When triangle vertices are composed of either profiler or other data that do not extend to the surface, the horizontal winds are estimated using data from the nearest grid point of the hourly Rapid Update Cycle (RUC; Benjamin et al. 2004) surface analyses closest to the central time of the time–space-corrected dataset. This is necessary for all profiler data, since the lowest gate is 500 m AGL. The remaining 10-hPa levels without data are filled using linear vertical interpolation between the RUC horizontal winds at the greatest (nearest to surface) pressure level and the pressure level at which the BAMEX field data or profiler data begin. When the depth of the vertical interpolation required exceeds 75 hPa, the vertical profiles of horizontal winds are not used to form triangles for the analysis.

The triangle size and obliqueness selection criteria are adjusted only slightly from those used for the relative vorticity analysis of Part I. The minimum acute angle between triangle legs must exceed 22.5° (0.4 rad) while the maximum leg length cannot exceed 250 km, and the area of the triangle must be between 4500 and 18 500 km$^2$. As noted in Part I, since a set of optimal triangles cannot be uniquely determined, we use all triangles that satisfy the general size and angle constraints. Figure 7a presents the centroid locations for criteria-meeting triangles used in the IOP 4 kinematic $\omega$ analysis and the time–space-corrected locations of dropsonde and profiler data from which these triangles were constructed. The number of such triangles ranged from 218 for IOP 5 to 1221 for IOP 15 (Table 1), which is primarily the result of differences in the number of profiler observations used.

After $\omega(p)$ has been calculated using (1) for all suitable triangles, a standard deviation $\omega_\sigma$ is calculated based on $\omega$ values at the same pressure level from other triangle centroids within 50 km of the current triangle centroid. We believe this provides some measure of representativeness of each $\omega$ value in lieu of using more stringent triangle selection criteria.

Both $\omega$ and $\omega_\sigma$ are gridded on constant pressure surfaces, every 10 hPa from 990 to 600 hPa, with a horizontal grid spacing of $\Delta x, y = 25$ km using the Gaussian weighting function,

$$\omega(x, y) = \sum_j \omega_j \exp(-a_j^2/R^2) \Big/ \sum_j \exp(-a_j^2/R^2), \tag{3}$$

where the index $j$ spans all triangle centroids, and $\omega_j$ and $a_j$ are the kinematic vertical velocity values at triangle centroids and their distances from the grid point, respectively. Here $R$ is set to 50 km in (3), which is ~0.75 of the mean original data spacing, as recommended by Spencer et al. (1999). To avoid unreasonable extrapolation of gridded data fields beyond where a reliable density of observations occur, these data are manually contoured after grid points are flagged as missing data when one or more triangle centroids do

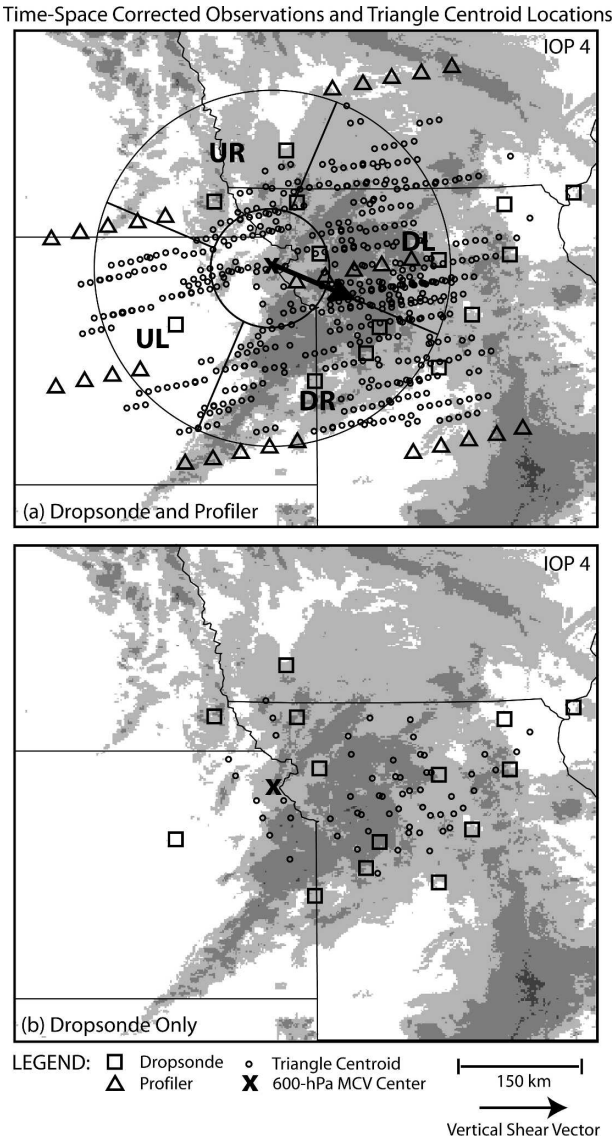


FIG. 7. Spatial distribution of observations and Bellamy triangle centroids used in the analysis of (a) kinematic and (b) isentropic vertical velocity for the example case of IOP 4. The range rings in (a) are located at 0.5 and 1.5 times the distance of the approximate RMW from the center of the MCV (Table 2). Objectively analyzed data within these range rings located in the DR, DL, UL, and UR quadrants are used to construct the vertical profiles of kinematic and thermodynamic quantities discussed in the text. The arrow in (a) schematically indicates the direction and magnitude of the 900–600-hPa environmental vertical shear (Table 2) with the "x" at the arrow tail denoting the approximate position of the 600-hPa MCV center (Table 2). Gray shades indicate composite radar reflectivity as in Fig. 3a.

TABLE 1. Number of different types of wind data measurements used to construct the Bellamy triangles, which were employed to diagnose the pressure vertical velocity $\omega$. The number of triangles used in the kinematic $\omega$ calculation that used all available observations (IOP 4 example shown in Fig. 7a) appears in the second column. The numbers of triangles used in the kinematic $\omega_K$ and isentropic $\omega_I$ analyses that excluded profiler observations (IOP 4 example shown in Fig. 7b) appear in the third column.

| | Bellamy triangles | | Observations | | | | |
|---|---|---|---|---|---|---|---|
| Case | Tot | Nonprofiler | Dropsonde | MGLASS | NWS sounding | NPN profiler | Tot |
| IOP 1 | 1013 | 241 | 16 | 0 | 0 | 20 | 36 |
| IOP 4 | 577 | 59 | 13 | 0 | 0 | 29 | 42 |
| IOP 5 | 218 | 139 | 12 | 2 | 1 | 5 | 20 |
| IOP 8 | 923 | 153 | 21 | 0 | 0 | 30 | 51 |
| IOP 15 | 1221 | 33 | 10 | 3 | 3 | 32 | 48 |

not occur within 50 km of the grid point. In section 4 we present analyses of $\omega$ and its normalized standard deviation, $\omega_\sigma/|\overline{\omega}|$, where $|\overline{\omega}|$ is the average magnitude of the gridded $\omega$ field.

An expression for the component of vertical velocity associated with the steady, isentropic, vortex-relative flow (Fig. 1) may be derived starting with the thermodynamic energy equation,

$$\frac{D\theta}{Dt} = \frac{\partial\theta}{\partial t} + \mathbf{V}\cdot\boldsymbol{\nabla}_p\theta + \omega\frac{\partial\theta}{\partial p}. \tag{4}$$

Under steady, adiabatic conditions, (4) reduces to

$$\omega = \frac{-\mathbf{V}\cdot\boldsymbol{\nabla}_p\theta}{\partial\theta/\partial p}. \tag{5}$$

Using the hydrostatic approximation and a $p \rightarrow \theta$ vertical coordinate transformation, it can be shown that (5) is equivalent to

$$\omega = \mathbf{V}\cdot\boldsymbol{\nabla}_\theta p.$$

This component of vertical velocity is often referred to as isentropic upglide or downglide depending on whether the flow is up or down the isentropic surface.

Using (5), the vortex-relative component of the steady, isentropic vertical motion, hereafter referred to as simply isentropic vertical motion, is estimated at triangle centroids by

$$\omega_I = \frac{a\overline{u_{\rm rel}} + b\overline{v_{\rm rel}}}{c(\overline{\partial\theta/\partial p})}, \tag{6}$$

where

$$\begin{aligned} a &= y_1(\theta_2-\theta_3) + y_2(\theta_3-\theta_1) + y_3(\theta_1-\theta_2)\\ b &= \theta_1(x_2-x_3) + \theta_2(x_3-x_1) + \theta_3(x_1-x_2)\\ c &= x_1(y_2-y_3) + x_2(y_3-y_1) + x_3(y_1-y_2). \end{aligned} \tag{7}$$

In (6), $\overline{u_{\rm rel}}$, $\overline{v_{\rm rel}}$, and $-\overline{\partial\theta/\partial p}$ are, respectively, the mean vortex-relative zonal and meridional wind components and static stability resulting from average values at the three triangle vertices. The triangle vertices are denoted by the subscripts on the right-hand side of (7). The coefficients $a$, $b$, and $c$ on the left-hand side of (7) are components of a vector normal to the plane (in $x$, $y$, $\theta$ space) defined by the three triangle vertices and a constant pressure surface.

Note that calculating isentropic vertical velocity, $\omega_I$, using (6) and (7) requires both vortex-relative horizontal winds and thermodynamic data at each triangle vertex. This significantly reduces the range and density of triangles (Fig. 7b) from those of the previous kinematic $\omega$ analysis (Fig. 7a), which also employs profiler winds (Table 1).

As for $\omega$ and $\omega_\sigma$, diagnosed values of $\omega_I$ and its standard deviations are then gridded using (3) and manually analyzed. A similar gridding and manual contouring procedure is also applied to thermodynamic quantities in the composite time–space-corrected dataset including potential temperature, water vapor mixing ratio, relative humidity (RH), equivalent potential temperature, and the lifted index (LI).[1] Here, LIs use 100-hPa-deep surface-based average virtual potential temperature and the water vapor mixing ratio and are evaluated at 500 hPa.

In addition to analyses on constant pressure surfaces, horizontally averaged downshear and upshear $\omega$ and potential temperature and humidity profiles are constructed using the $\Delta p = 10$ hPa gridded analyses. The geometry used for this calculation is displayed in Fig. 7a. Downshear and upshear sectors are defined with the orientation of the 900–600-hPa environmental wind shear vector as the abscissa. These sectors are required to lie within the radius range (indicated by the area within the two rings in Fig. 7a) of 0.5–1.5 times the radius of maximum wind (RMW) of the 600-hPa vortex, whose center defines the origin of the coordinate

[1] LIs are used in place of a vertically integrated buoyancy measure, such as the convective available potential energy, since reliable dropsonde data begin at ~250 hPa, well beneath the tropopause.

system. The environmental shear and the RMW (Table 2) were estimated in Part I.

Recall that the gridding procedure described earlier requires at least one upper air observation occurring within 50 km of the grid point for a value to be assigned. Thus, the gridded data coverage exhibits some variation within the individual downshear and upshear sectors due to irregularities in the spatial distribution of the data. For example, the upshear right (UR) quadrant from IOP 4 contains significantly fewer kinematic $\omega$ triangle centroids than the upshear left (UL) quadrant (Fig. 7a). To prevent sectors from being dominated by a larger number of available grid points from a single quadrant, the gridded data are first averaged by quadrant. The two quadrants for each sector are then averaged to produce the vertical profiles. Table 3 indicates the number of grid point values available in the different quadrants for the vertical profile calculations of various kinematic and thermodynamic quantities.

Like thermodynamic vertical structure, the MCV can locally modify the vertical shear, which can in turn modulate the organization and intensity of deep convection. Analyses of the magnitude and the zonal and meridional components of vertical shear are constructed for four different MCV sectors. These include downshear and upshear (as before) and the sectors to the right and left of the environmental vertical shear, which comprise the UL and downshear right (DR) quadrants (Fig. 7a), and the UR and downshear left (DL) quadrants (Fig. 7a), respectively. Here the vertical shear is defined by the differences between the horizontal winds at 350 hPa above the surface pressure and the horizontal winds averaged over the lowest 100 hPa AGL.[2]

TABLE 2. Vortex and environmental vertical shear parameters used in the calculation of downshear- and upshear-averaged vertical profiles presented in Figs. 9–11 (see section 3 for details). The MCV RMWs are in km. Latitude (LAT) and longitude (LON) of the MCV centers and the azimuth of the vertical shear are in degrees. The vertical shear magnitudes are in m s$^{-1}$.

| | | 600-hPa MCV center | | 900–600-hPa vertical shear | |
|---|---|---|---|---|---|
| Case | RMW | LAT | LON | Azimuth | Magnitude |
| IOP 1 | 100 | 35.75 | −93.00 | 301 | 14.9 |
| IOP 4 | 150 | 39.50 | −95.50 | 293 | 15.8 |
| IOP 5 | 100 | 32.50 | −96.25 | 277 | 13.7 |
| IOP 8 | 150 | 36.50 | −92.00 | 267 | 1.8 |
| IOP 15 | 100 | 38.50 | −98.00 | 257 | 7.3 |

## 4. Mesoscale vertical motions in the MCV environment

### *a. Lower-tropospheric horizontal structure*

Kinematic $\omega$ is displayed at 800 hPa for IOPs 1, 4, 5, and 8 (Figs. 8a–d) and at 750 hPa for IOP 15 (Fig. 8e). These pressure levels are located above the PBL, where thermodynamic structure (section 5) is strongly influenced by vertical displacements, but are close enough to the lower boundary so that $\omega$ is unlikely to be strongly influenced by systematic divergence errors that may accumulate in an upward integration of (1). Here, mesoscale vertical motions (Fig. 8) appear related to both the environmental vertical shear and the precipitation within the MCV.[3]

Cases with only localized precipitation and moderate (IOP 15) or strong (IOP 5) environmental vertical shear have well-defined vertical motion couplets (Figs. 8c,e). Here, ascent ($\omega < 0$) downshear and subsidence ($\omega > 0$) upshear from the MCV center are consistent with idealized (dry) numerical simulations (e.g., Raymond and Jiang 1990; Trier et al. 2000b).

In cases where widespread stratiform precipitation persists within the MCV (IOPs 1 and 4), maximum mesoscale upward motion is located downshear but closer to the MCV center (Figs. 8a,b) than in the previous two cases. Here, the maximum lower-tropospheric ascent nearly coincides with the most intense stratiform precipitation itself, particularly in IOP 4 (Fig. 8b). This situation differs from previous studies, where unsaturated mesoscale downdrafts were diagnosed in stratiform regions of mature-to-decaying MCSs, within which the MCVs had developed (Brandes 1990; Jorgensen and Smull 1993). In IOPs 1 and 4, lower-tropospheric conditions are nearly saturated (not shown), and condensational warming should overwhelm evaporative cooling. Here, latent heat release likely enhances mesoscale ascent, which appears to be strongly forced by convergence along lower-tropospheric frontal zones (Part I, their Figs. 5a,b).

The most intense vortex (IOP 8), which occurs in weak environmental vertical shear (Table 2), has precipitation and mesoscale vertical motion patterns that

[2] The minor change from the 600–900-hPa shear layer (relevant to MCV-induced vertical motions above the PBL) is designed to account for frictional turning of the PBL winds beneath 900 hPa, which can contribute significantly to the vertical shear in the inflow to convection.

[3] Both the precipitation and mesoscale vertical motions within the MCVs are also influenced by the different sampling times relative to the decay of the antecedent MCS, which varies from a few hours afterward (IOP 1) to 12 h after such decay (IOP 15).

TABLE 3. Number of grid points (by quadrant) used to create sector averages for the vertical profiles of kinematic pressure vertical velocity $\omega$ (Fig. 9), potential temperature $\theta$ (Fig. 10), RH (Fig. 11), and the local vertical shear (Fig. 18). The relationship between the quadrants and the environmental vertical shear vector is illustrated for the IOP 4 case in Fig. 7a. The averaging procedure for the objectively analyzed data is described in section 3.

| | | Quadrant grid points used in averages for vertical profiles | | | | | | | | | | | |
|---|---|---|---|---|---|---|---|---|---|---|---|---|---|
| | | Kinematic $\omega$ | | | | $\theta$, RH | | | | Vertical shear | | | |
| Case | RMW | DR | DL | UR | UL | DR | DL | UR | UL | DR | DL | UR | UL |
| IOP 1 | 100 | 25 | 26 | 25 | 24 | 9 | 26 | 22 | 5 | 11 | 22 | 20 | 13 |
| IOP 4 | 150 | 58 | 58 | 27 | 53 | 25 | 31 | 31 | 9 | 34 | 40 | 38 | 29 |
| IOP 5 | 100 | 23 | 25 | 22 | 23 | 19 | 23 | 22 | 17 | 15 | 19 | 18 | 13 |
| IOP 8 | 150 | 50 | 60 | 48 | 50 | 41 | 39 | 27 | 40 | 35 | 47 | 39 | 36 |
| IOP 15 | 100 | 25 | 25 | 25 | 25 | 18 | 17 | 16 | 23 | 18 | 18 | 14 | 26 |

are distinct from the two previously discussed sets of cases. Mesoscale upward motion is most concentrated within the RMW with subsidence common toward the edges of the MCV circulation (Fig. 8d). An exception occurs along the southeastern periphery of the MCV where poorly resolved upward motion is associated with strong convection.

### *b. MCV regional vertical profiles*

The downshear and upshear kinematic $\omega$ vertical profiles exhibit significant variation among the IOPs (Fig. 9). On average, downshear ascent occurs from the lower troposphere through 600 hPa, with weaker upshear subsidence restricted to above 800 hPa (Fig. 9a). There are several likely contributors to this asymmetry in the downshear/upshear profiles. First, latent heat release in precipitation contributes to ascent. Cases where widespread stratiform precipitation occurs (Figs. 8a,b) have either both downshear and upshear ascent (IOP 4; Fig. 9c) or significant downshear ascent with approximately neutral vertical motion upshear (IOP 1; Fig. 9b). Even in IOP 5 (Fig. 9d), where precipitation is less widespread, it is likely that the larger magnitude of the downshear vertical motion is influenced by convection given that the maximum ascent approximately coincides with the secondary convection (Fig. 8c).

The vertical motion asymmetry in the five-case composite (Fig. 9a) is also influenced by the vertical tilt of the MCV circulation. Since the downshear and upshear locations are defined relative to where the vortex is strongest (600 hPa), a portion of the "upshear" region in Fig. 9 can be located downshear relative to the vortex center at lower levels in some cases. IOP 5 has the largest downshear vortex tilt (Part I, their Fig. 6c). Here, the tilt may partly explain the upshear ascent at 900 hPa with upshear descent at 600 hPa (Fig. 9d). This influence of vortex tilt on the vertical motions is similar to that described in the idealized simulations of Trier et al. (2000b), where it was concluded that such tilt biases the maximum lower-tropospheric ascent from downshear near the RMW to closer to the center of the midtropospheric vortex. More symmetric vertical motion profiles occur in IOP 15 (Fig. 9f), which like IOP 5, has only localized downshear precipitation, but exhibits lesser vortex tilt above 800 hPa (Part I, their Fig. 6e), consistent with weaker environmental shear (Table 2).

IOP 8 is unique with negligible differences between mean upshear and downshear vertical motions (Fig. 9e). We speculate that this is due largely to the weakness of the environmental vertical shear (Table 2). Significant cancellations of $\omega$ occur within individual upshear and downshear sectors as evinced by the small amplitudes of $\omega$ in the regional vertical profiles (Fig. 9e) despite several well-defined centers of mesoscale vertical motion within the MCV (Fig. 8d).

Perturbation potential temperature, $\theta'$ (Fig. 10), and relative humidity (Fig. 11) vertical profiles exhibit differences between upshear and downshear sectors that are generally consistent with the previously discussed $\omega$ differences (Fig. 9). For instance, lesser dry static stability, $-\partial\theta'/\partial p$, downshear in the 825–650-hPa layer for the five-case composite (Fig. 10a) is consistent with differences in adiabatic cooling associated with $\partial\omega/\partial p > 0$ downshear and $\partial\omega/\partial p < 0$ upshear within this layer (Fig. 9a). The static stability differences above the PBL between the downshear and upshear locations are greatest in IOP 5 (Fig. 10d), where such regional differences in $\partial\omega/\partial p$ are greatest (Fig. 9d). In IOPs 1 (Fig. 10b) and 4 (Fig. 10c), the downshear–upshear differences in the vertical structure of $\theta'$ are less striking and are superimposed on more significant horizontal variations associated with large-scale gradients (not shown). Lower relative humidity above ~750 hPa upshear in both the five-case composite (Fig. 11a) and individual cases (Figs. 11b–f) is consistent with greater subsidence (or smaller ascent) upshear than downshear. On average,

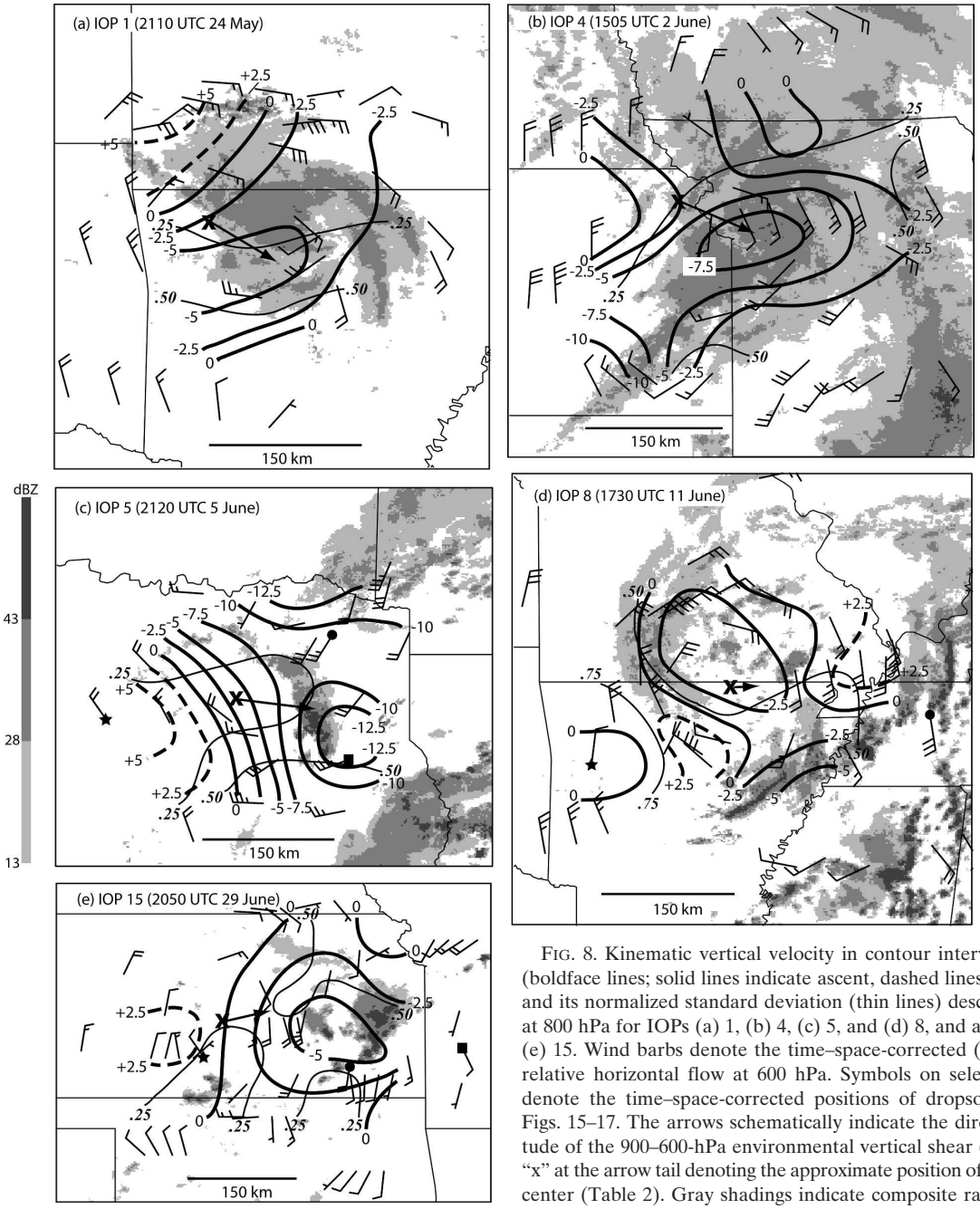


FIG. 8. Kinematic vertical velocity in contour intervals of 2.5 $\mu$b s$^{-1}$ (boldface lines; solid lines indicate ascent, dashed lines indicate descent) and its normalized standard deviation (thin lines) described in section 3 at 800 hPa for IOPs (a) 1, (b) 4, (c) 5, and (d) 8, and at 750 hPa for IOP (e) 15. Wind barbs denote the time–space-corrected (see Part I) MCV-relative horizontal flow at 600 hPa. Symbols on selected observations denote the time–space-corrected positions of dropsondes analyzed in Figs. 15–17. The arrows schematically indicate the direction and magnitude of the 900–600-hPa environmental vertical shear (Table 2) with the "x" at the arrow tail denoting the approximate position of the 600-hPa MCV center (Table 2). Gray shadings indicate composite radar reflectivity.

conditions within the PBL (i.e., below 850 hPa), where mesoscale vertical motions are relatively weak (Fig. 9), are both warmer (Fig. 10a) and, with comparable relative humidity (Fig. 11a), moister (in an absolute sense) downshear than upshear.

### c. *Isentropic vertical motions*

The foregoing analysis has illustrated a strong relationship between vertical shear and vertical motion, particularly for MCVs occurring in at least moderate vertical shear with only localized downshear precipitation (e.g., IOPs 5 and 15). We now seek to determine the contribution that the isentropic component (Fig. 1) provides to the overall vertical motion.

Unlike for the kinematic $\omega$ analyses, the triangle centroids used to construct the gridded analyses of $\omega_I$ fall almost entirely within the RMW (cf. Figs. 7a,b) of each MCV. Therefore, unlike for kinematic $\omega$, these analyses

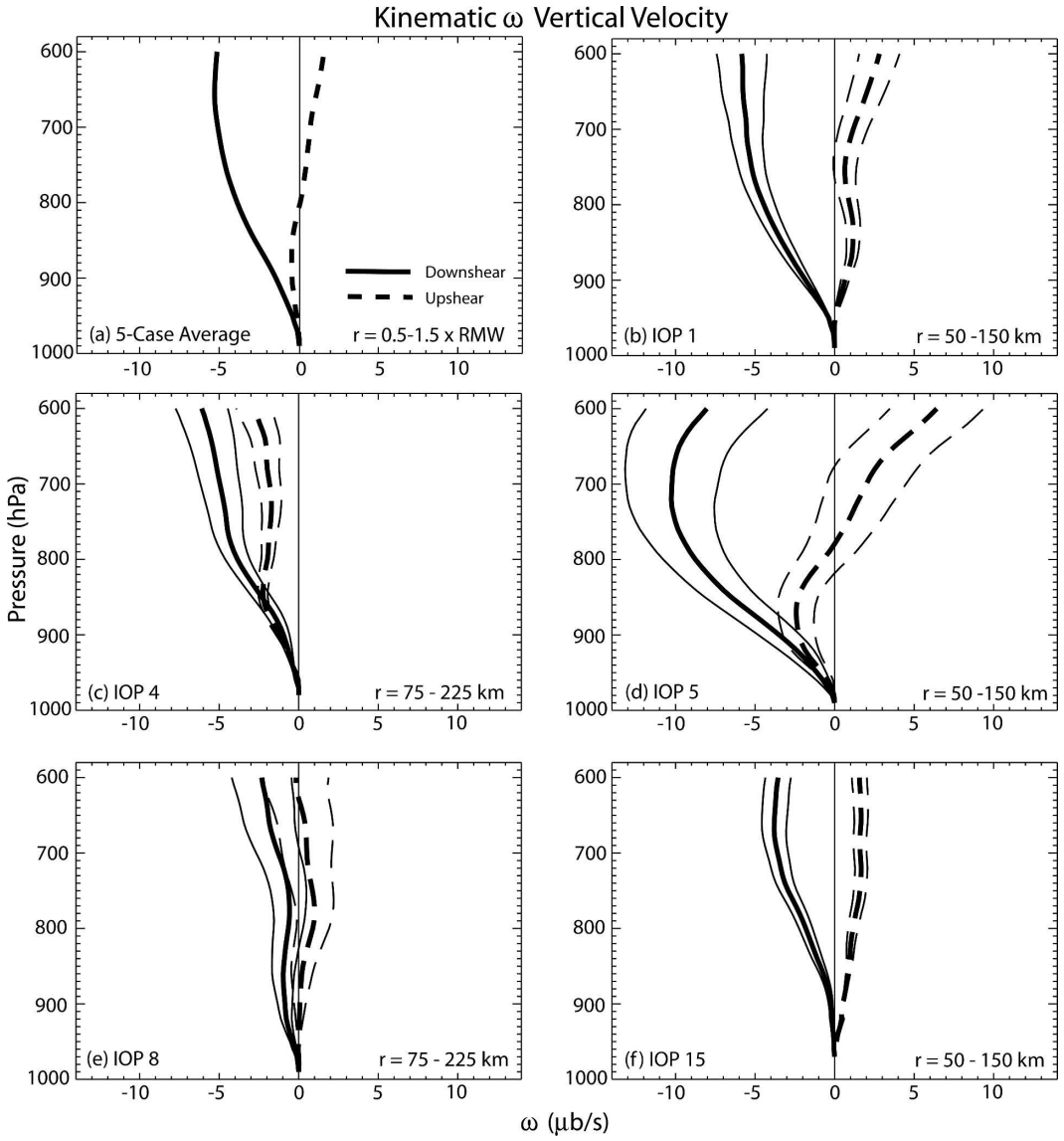


FIG. 9. Vertical profiles of kinematic vertical velocity averaged radially and azimuthally between 0.5 and 1.5 times the approximate distance of the RMWs from the 600-hPa MCV center (Table 2) for downshear (solid) and upshear (dashed) regions of the MCV circulation. The boldface lines denote $\omega$ area means and thin lines encompass the area-average standard deviation $\omega_\sigma$ for the gridded pressure-level data (see section 3) that make up the downshear and upshear regions: (a) five-case average and IOPs (b) 1, (c) 4, (d) 5, (e) 8, and (f) 15.

are insufficient to construct downshear and upshear $\omega_I$ vertical profiles that span the majority of the MCV circulation. However, gridded pressure-level analyses of $\omega_I$ may be compared to additional analyses of the kinematic pressure vertical velocity, $\omega_K$, generated, for consistency, using the identical reduced set of triangles (Table 1).

Kinematic analyses constructed from the reduced dataset (Figs. 12a–e) are similar to those using the full composite dataset (Figs. 8a–e), where the profiler data serve primarily to extend the analyses out beyond the RMW. Within the RMW, $\omega_K$ differs significantly from $\omega$ only in IOP 8 (cf. Figs. 8d, 12d). However, the $\omega_K$ analyses generally have larger normalized standard deviations (section 3) than the $\omega$ analyses.

The lower-tropospheric $\omega_I$ pattern conforms to the balanced MCV vertical motion pattern conceptualized by Raymond and Jiang (1990) in four of the five IOPs. In these cases (IOPs 4, 5, 8, and 15), lower-tropospheric ascent occurs downshear with subsidence upshear from the MCV center (Figs. 12g–j), where warm and cold advections, respectively, occur (Part I, their Figs. 5b–e).

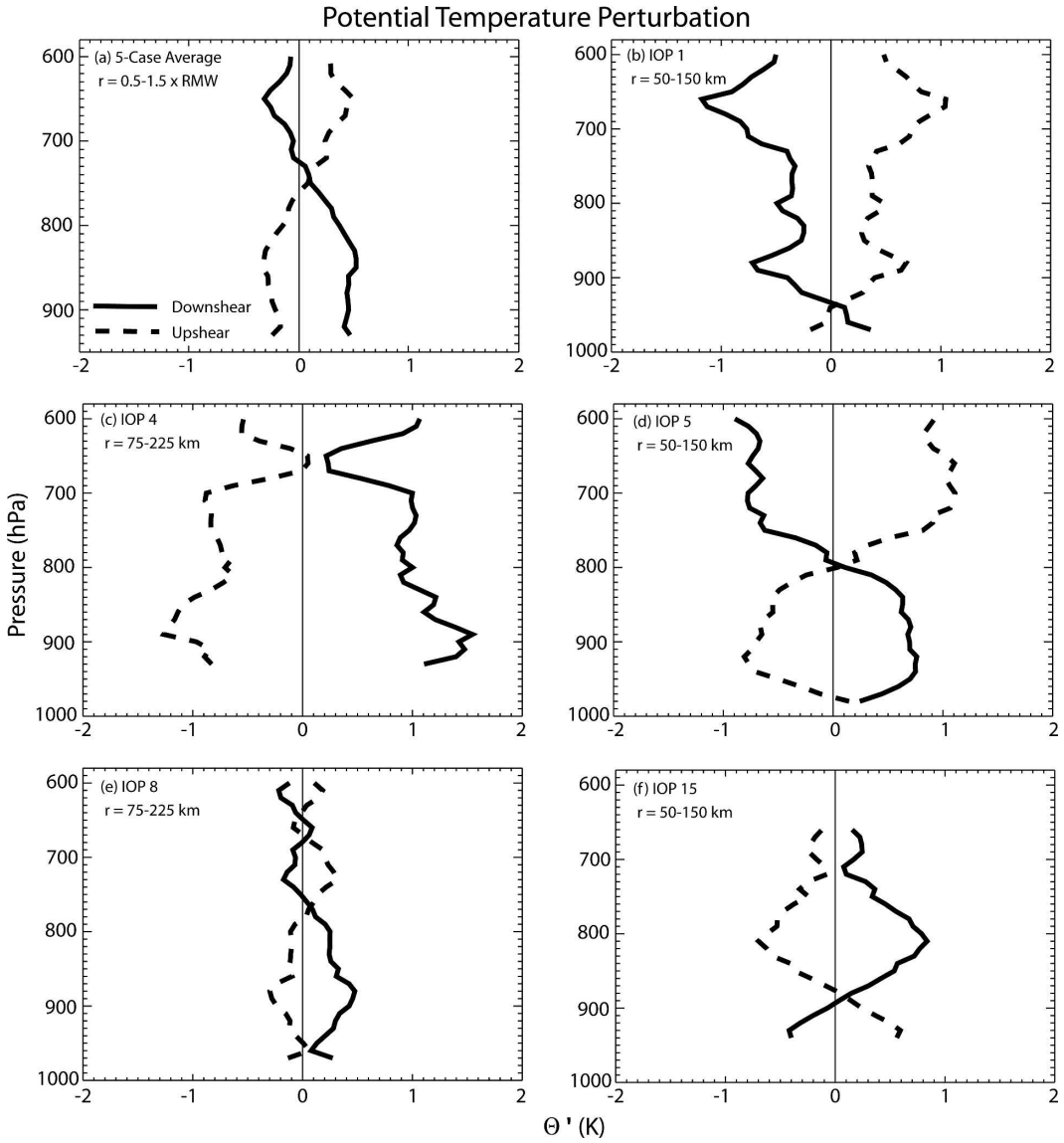


FIG. 10. As in Fig. 9 but for the area means of potential temperature perturbation, where the mean subtracted from upshear and downshear sectors (located between 0.5 and 1.5 times the RMWs) is area averaged from the vortex center out to 1.5 times the RMWs.

Note, however, that the upshear isentropic descent region is poorly sampled in some of the cases. For example, in IOP 5 (Fig. 12h), thermodynamic data are only sufficient to indicate a small region of very weak isentropic descent ($0 < \omega_I < 0.5$ $\mu$b s$^{-1}$). The large downshear vertical tilt of this vortex, discussed earlier (section 4b), made it difficult to sample in its entirety. Thus, it is possible that stronger isentropic descent may have occurred farther west, beyond the range of the data. In IOPs 4 and 5, the warm advection and hence lower-tropospheric isentropic ascent (Figs. 12g,h) on the downshear side is clearly enhanced by the environmental baroclinity in which the MCV is embedded (Part I, their Figs. 5b, c), whereas in IOP 8, the strength of the vortex flow results in significant isentropic ascent on the downshear side (Fig. 12i) despite relatively weak environmental baroclinity (Part I, their Fig. 5d).

Overall, the lower-tropospheric isentropic vertical motions (Figs. 12f–j) are considerably weaker than kinematically derived vertical motions (Figs. 12a–e), with the amplitude of $\omega_I$, on average, only ~0.25 the amplitude of $\omega_K$ (Table 4). Despite weaker amplitudes, the $\omega_I$ patterns resemble the $\omega_K$ patterns in IOPs 5 (Figs. 12c,h) and 15 (Figs. 12e,j), where the environmental

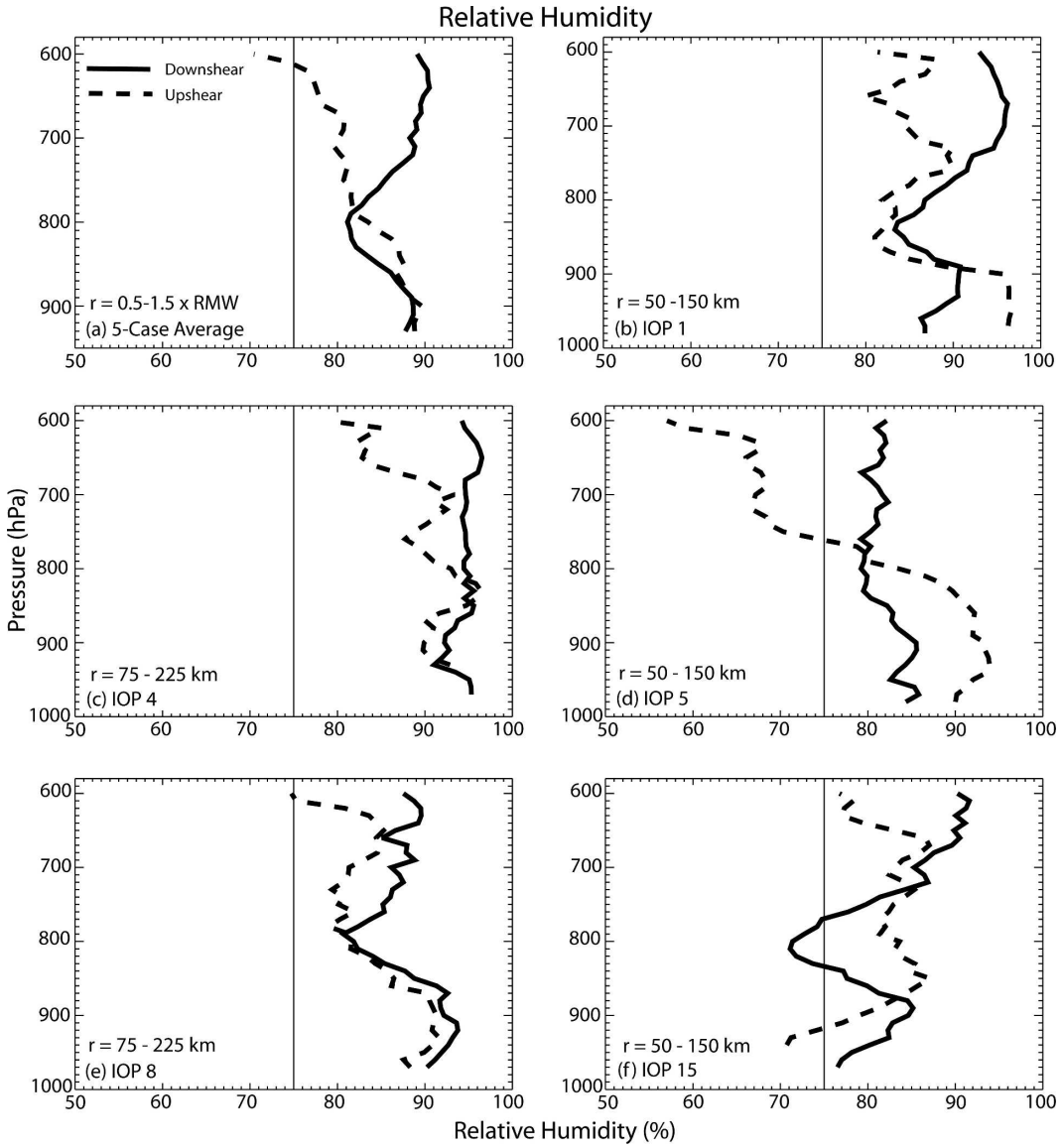


FIG. 11. As in Fig. 9 but for the area means of relative humidity.

vertical shear is at least moderately strong and precipitation within the MCV circulation is not widespread. This is demonstrated quantitatively using linear correlation coefficients,

$$r = \frac{\sum \omega'_K \omega'_I}{\sqrt{\sum \omega'^2_K}\sqrt{\sum \omega'^2_I}}, \tag{8}$$

between the two fields (primes indicate deviations from mean values), where a moderate-to-strong correlation $r = 0.57$ occurs for IOP 5 and a moderate correlation $r = 0.36$ for IOP 15 (Table 4). Correlations are poor ($r < 0.2$) for the other 3 cases (Table 4), which suggests the importance of factors not included in the derivation of (6) and (7), including diabatic processes and local temporal changes in potential temperature.

Both diabatic processes and local changes likely contribute to the significant amplitude differences between $\omega_K$ and $\omega_I$, even in the cases where their patterns are reasonably well correlated (IOPs 5 and 15). For example, in IOP 5, the strongest kinematic ascent occurs in the vicinity of convection, which could contribute to the large amplitude of $\omega_K$. IOP 5 also departs from the conceptual model of Fig. 1 in that it is a strongly tilted vortex (Part I, their Fig. 5c). In such cases, shear-induced evolution of the isentropic surfaces (e.g., Raymond 1992) can also contribute to the total vertical motion.

## 5. MCV influences on precipitation organization

In this section, we explore the thermodynamic vertical structure and vertical wind shear differences across the MCV circulations, with an emphasis on how both the vertical and horizontal motions within the MCV can focus secondary convection.

### *a. Conditional instability of the PBL*

The strongest convection in IOPs 8 (Fig. 13d) and 15 (Fig. 13e) develops along the downshear periphery of the MCV circulation where conditions are most unstable with LIs from $-2°$ to $-5°$C. These two cases contrast with IOP 5 (Fig. 13c), where the surface-based conditional instability is both less, with minimum LIs of only slightly below 0°C, and more localized. Here, both the maximum conditional instability and the secondary convection occur closer to the MCV center where mesoscale lifting is strong (Fig. 8c). Although widespread heavy precipitation occurs within the MCV circulation in IOPs 1 (Fig. 13a) and 4 (Fig. 13b), these cases have conditionally stable environments with little or no convection.

Excluding cases with weak environmental vertical shear (IOP 8) and significant large-scale forcing (IOP 4), a clear relationship exists between the degree of conditional instability and where, relative to the environmental vertical shear vector, heavy precipitation develops. The convection is entirely to the right of downshear in IOP 15, in which there is moderate conditional instability (Fig. 13e), whereas the heavy precipitation is left of downshear in IOP 1, in which there is no conditional instability (Fig. 13a). In IOP 5, where conditional instability is limited, convection is directly downshear (Fig. 13c). Since greater vertical displacements are usually required to produce heavy precipitation in stable environments than in conditionally unstable environments, this observed range of behavior is consistent with idealized dry simulations (Trier et al. 2000b). In those simulations, maximum lower-tropospheric vertical displacements are typically left of downshear, downstream from the maximum instantaneous vertical motions, which are right of downshear.

The primary role of mesoscale ascent in facilitating convection is to destabilize specific locations within the MCV because of adiabatic cooling above the PBL, which can increase the low–midtropospheric lapse rate and relative humidity. Similarly, mesoscale subsidence stabilizes specific regions through adiabatic warming, which can result in decreases of lapse rate and relative humidity. Horizontal advections of temperature and moisture can also focus convection in MCV environments. Thermodynamic destabilization occurs when mesoscale ascent overlies positive horizontal temperature and moisture advections, which together influence $\theta_e$. On the other hand, thermodynamic stabilization occurs when subsidence overlies negative advections of these quantities.

Horizontal advections can have a particularly strong influence on daytime convection when the MCV circulation penetrates into the PBL, where horizontal temperature and moisture contrasts are often quite large. Although maximum $\zeta$ within the MCVs occurs in the midtroposphere, $\zeta > 0$ is found within the PBL in each of the 5 IOPs (Part I, their Fig. 6). In one case, $\zeta > 0$ in the PBL is clearly associated with surface penetration of the midlevel MCV circulation (IOP 8), while in others (particularly IOPs 5 and 15), it may result primarily from the proximity of a surface frontal zone (see Part I).

Substantial variation of $\theta_e$ in the PBL occurs across the individual MCVs (Fig. 14), where maxima are approximately coincident with minimum LIs on the MCV's southeastern flank in IOPs 5, 8, and 15 (cf. Figs. 14c–e with Figs. 13c–e). Conversely, $\theta_e$ minima are found on the west side of the MCVs in IOPs 8 and 15 (Figs. 14d,e) where LIs are larger (Figs. 13d,e). Within the lower-tropospheric baroclinic zones in which these MCVs are generally embedded, $\theta_e$ increases from north to south. Thus, the elongated zones of high and low $\theta_e$ parallel to the vortex tangential flow on the eastern and western flanks of the MCV, respectively, illustrate the influence of the MCV on thermodynamic stability through differences in horizontal advections of temperature and moisture on these different sides of its circulation.

### *b. Thermodynamic vertical structure across the MCV*

Bulk differences in temperature and moisture structure between the downshear and upshear sectors were illustrated in the previous section (Figs. 10, 11). We now take a closer look at selected individual dropsondes deployed along the Lear jet flight tracks in secondary convection cases (IOPs 5, 8, and 15), which reveal both more detailed and dramatic regional differences across the MCV and within the individual downshear and upshear regions themselves.

#### 1) IOP 5

The limited spatial extent and magnitude of the midafternoon conditional instability in the downshear region of IOP 5 (Fig. 13c) is influenced by an east–west-oriented surface front in proximity to the MCV (Part I, their Fig. 5c) and the remnant thermodynamic struc-

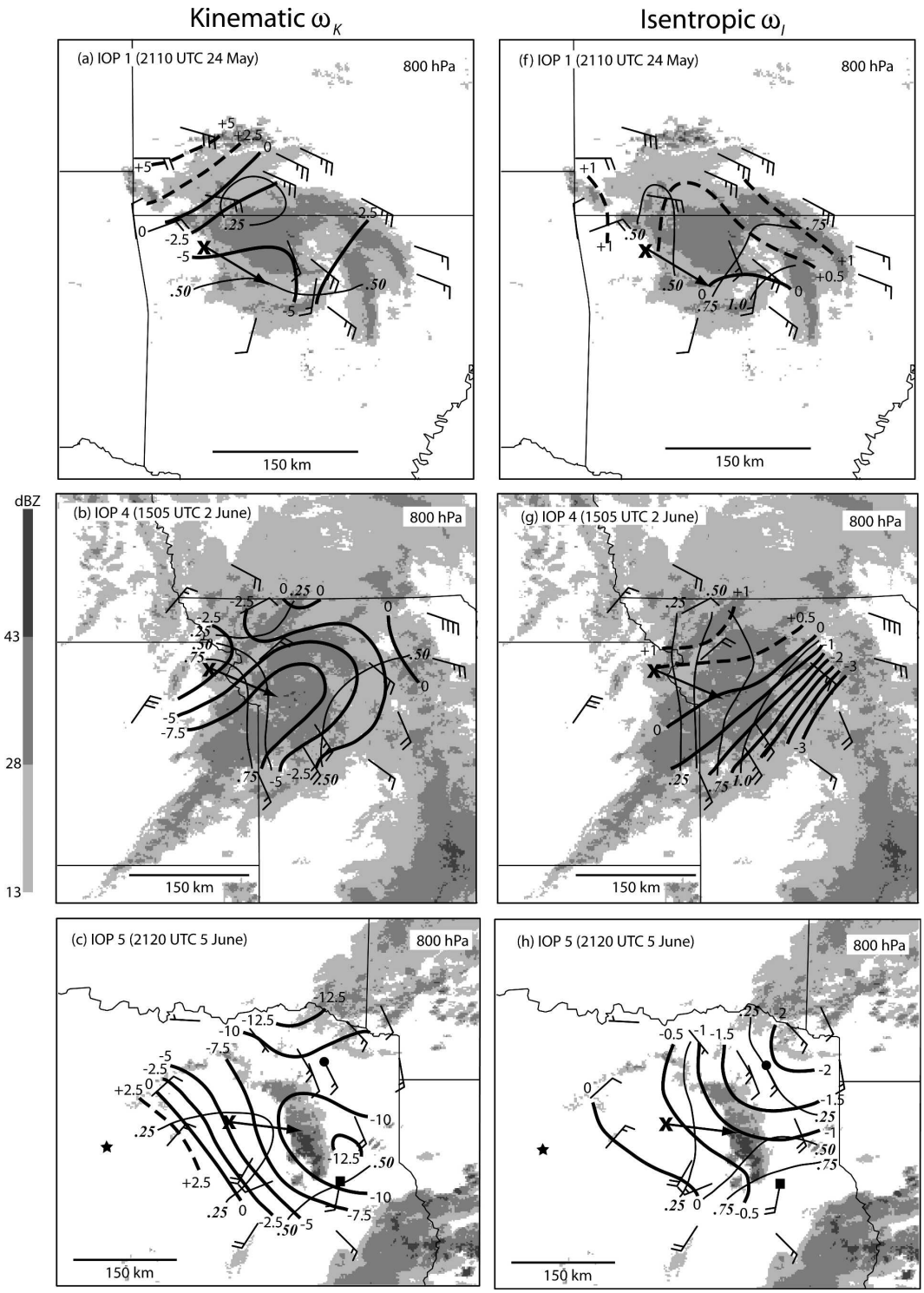


FIG. 12. (left) Kinematic vertical velocity in contour intervals of 2.5 $\mu$b s$^{-1}$ and its normalized standard deviation. (right) Vortex-relative isentropic vertical velocity (see section 3) in contour intervals of 0.5 $\mu$b s$^{-1}$ and its normalized standard deviation. Plots are as in Fig. 8 at 800 hPa for IOPs (a), (f) 1; (b), (g) 4; (c), (h) 5; and (d), (i) 8; and at 750 hPa for (e), (j) IOP 15 but using only dropsonde and rawinsonde observations for the analysis. Time–space-corrected MCV-relative horizontal winds plotted are at the same pressure levels. All other symbols are as in Fig. 8.

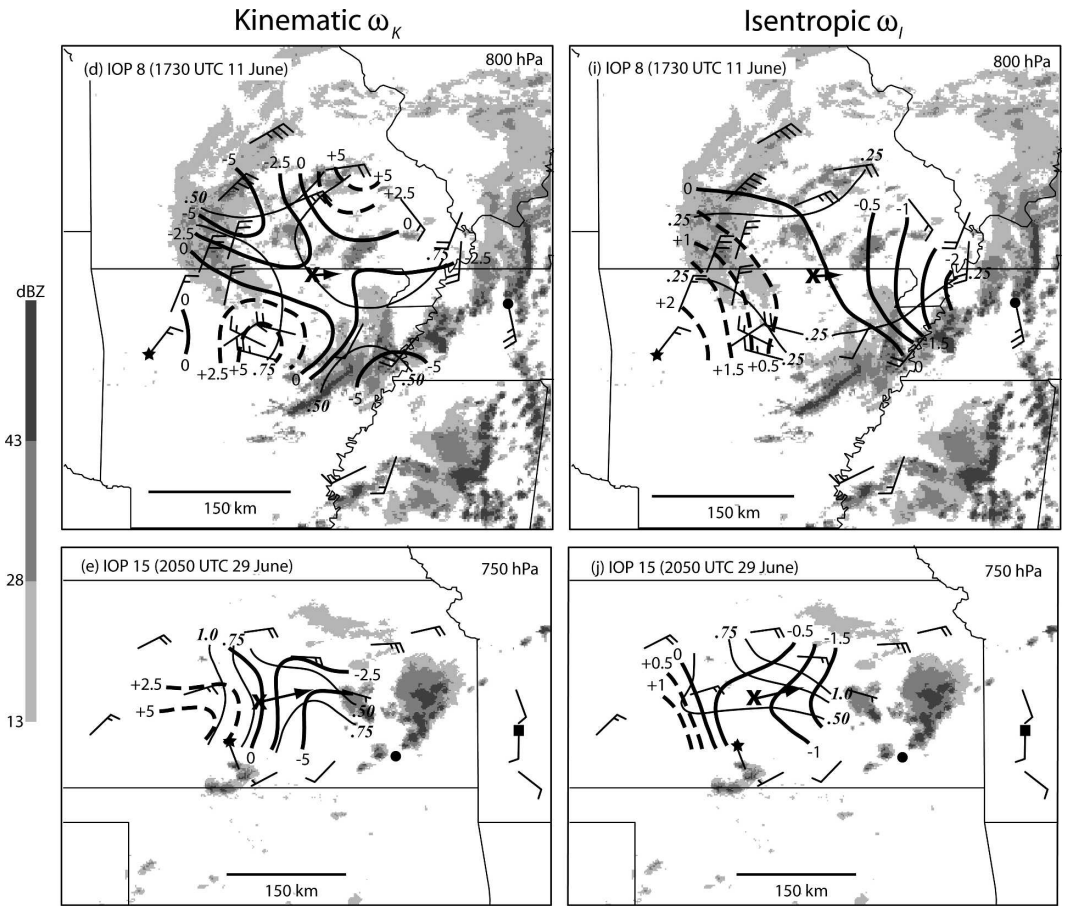


FIG. 12. (*Continued*)

tures of the previous large nocturnal MCS (Part I, their Fig. 3c) that spawned this MCV.

A downshear dropsonde deployed south of the surface baroclinic zone and ~50 km beyond the southern end of the convective line (square in Fig. 15a) exhibits a 75-hPa-deep surface-based conditionally unstable PBL (gray curves in Fig. 15b). However, the surface-based instability is limited by a midtropospheric dry inversion layer based near 550 hPa beneath the remnant ice anvil from the nocturnal MCS (Fig. 15a).

A second downshear dropsonde from near the northern end of the ~150-km-long quasi-stationary afternoon convective line (circle in Fig. 15a) at 2022 UTC is located within the surface-based baroclinic zone. In this sounding (black curves in Fig. 15b), the dry layer is based at 400 hPa (~150 hPa higher) and is no longer an impediment to deep convection. Beneath the frontal inversion the easterly flow is conditionally stable. However, a ~500-hPa-deep layer of modest temperature excess ($T' = 0$–3 K) over ambient air exists for air parcels originating within the nearly saturated 900–800-hPa layer immediately above the front (black curves in Fig. 15b). The moist conditionally unstable conditions within this layer are consistent with a long path of ascent that trajectories in the southeasterly flow immediately above the front would likely have experienced by the time they had reached the northern portion of the line (circles in Figs. 12c,h).

These two downshear dropsondes contrast dramatically with an upshear dropsonde taken from just be-

TABLE 4. Statistics of the gridded vertical velocity ($\mu$b s$^{-1}$) fields contoured in Fig. 12 diagnosed using the kinematic method $\omega_K$ (Figs. 12a–e) and assuming steady, vortex-relative isentropic motions $\omega_I$ (Figs. 12f–j). The linear correlation coefficient between the fields $r$ is calculated using Eq. (8).

| | Amplitude | | Mean | | Correlation |
|---|---|---|---|---|---|
| Case | $\omega_K$ | $\omega_I$ | $\omega_K$ | $\omega_I$ | $r(\omega_K, \omega_I)$ |
| IOP 1 | 3.95 | 0.69 | −1.30 | 0.54 | 0.18 |
| IOP 4 | 4.79 | 1.49 | −3.52 | −0.21 | 0.02 |
| IOP 5 | 8.75 | 1.21 | −7.51 | −0.94 | 0.57 |
| IOP 8 | 3.37 | 1.16 | −1.29 | 0.09 | 0.16 |
| IOP 15 | 3.40 | 1.27 | 0.53 | −0.55 | 0.36 |

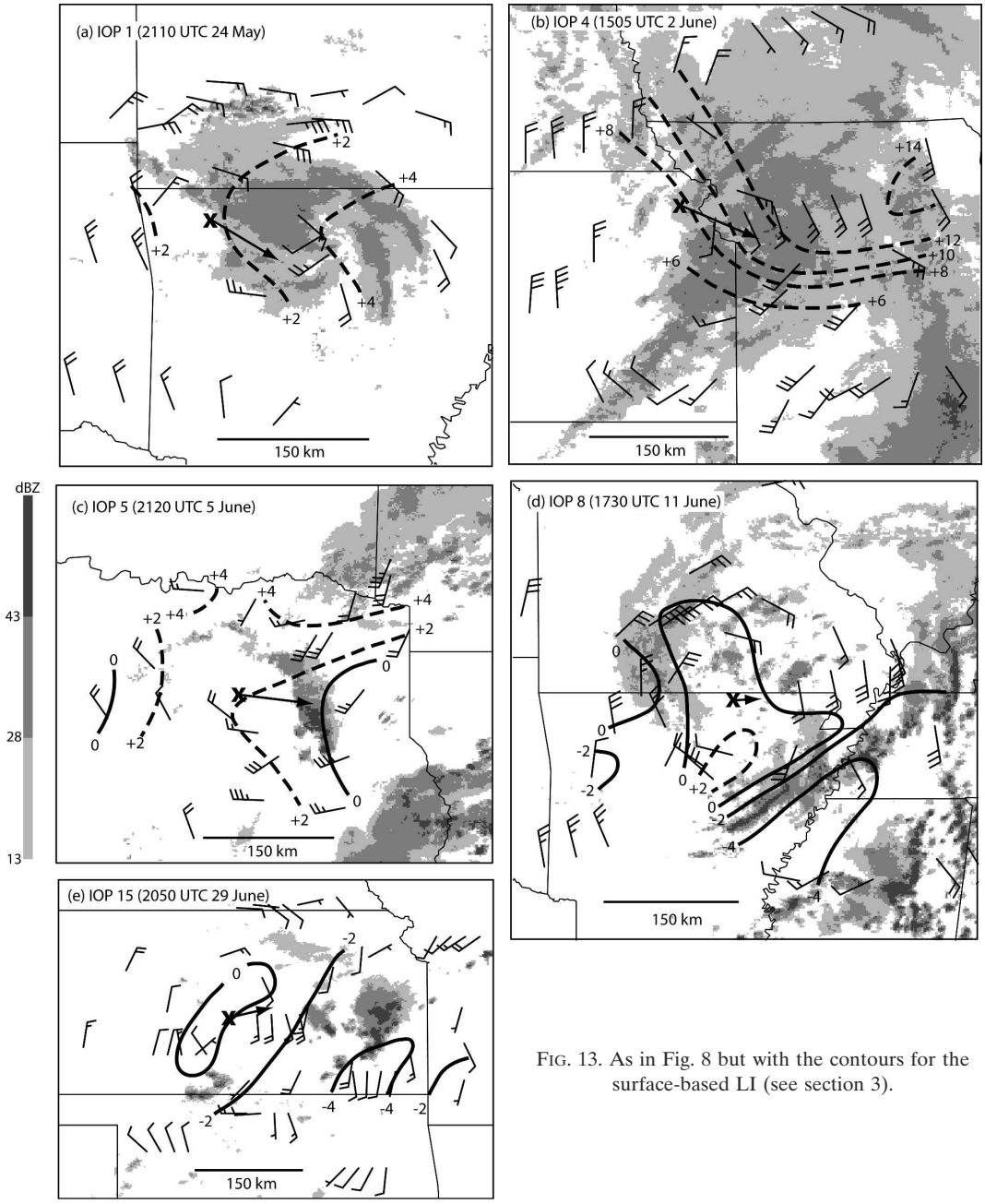


FIG. 13. As in Fig. 8 but with the contours for the surface-based LI (see section 3).

yond the western edge of the lower-tropospheric MCV cloud shield (star in Fig. 15a). Comparing the downshear dropsonde within the baroclinic zone (black curves in Fig. 15c) with the upshear dropsonde deployed 32 min later (gray curves in Fig. 15c) reveals major differences in the thermodynamic properties of the 750–400-hPa layer. The generally cooler and moister conditions downshear are consistent with the downshear ascent and upshear subsidence in the regional vertical profiles (Fig. 9d). Note that the air beneath the level of the upshear subsidence inversion from ~900 to 750 hPa has similar thermodynamic characteristics in both dropsondes, which strongly suggests the importance of mesoscale vertical motion above the layer of highest $\theta_e$ air in focusing the limited deep convection.

### 2) IOP 15

In IOP 15, a conditionally unstable PBL ~300 km east of the MCV center (gray curves in Fig. 16b) is

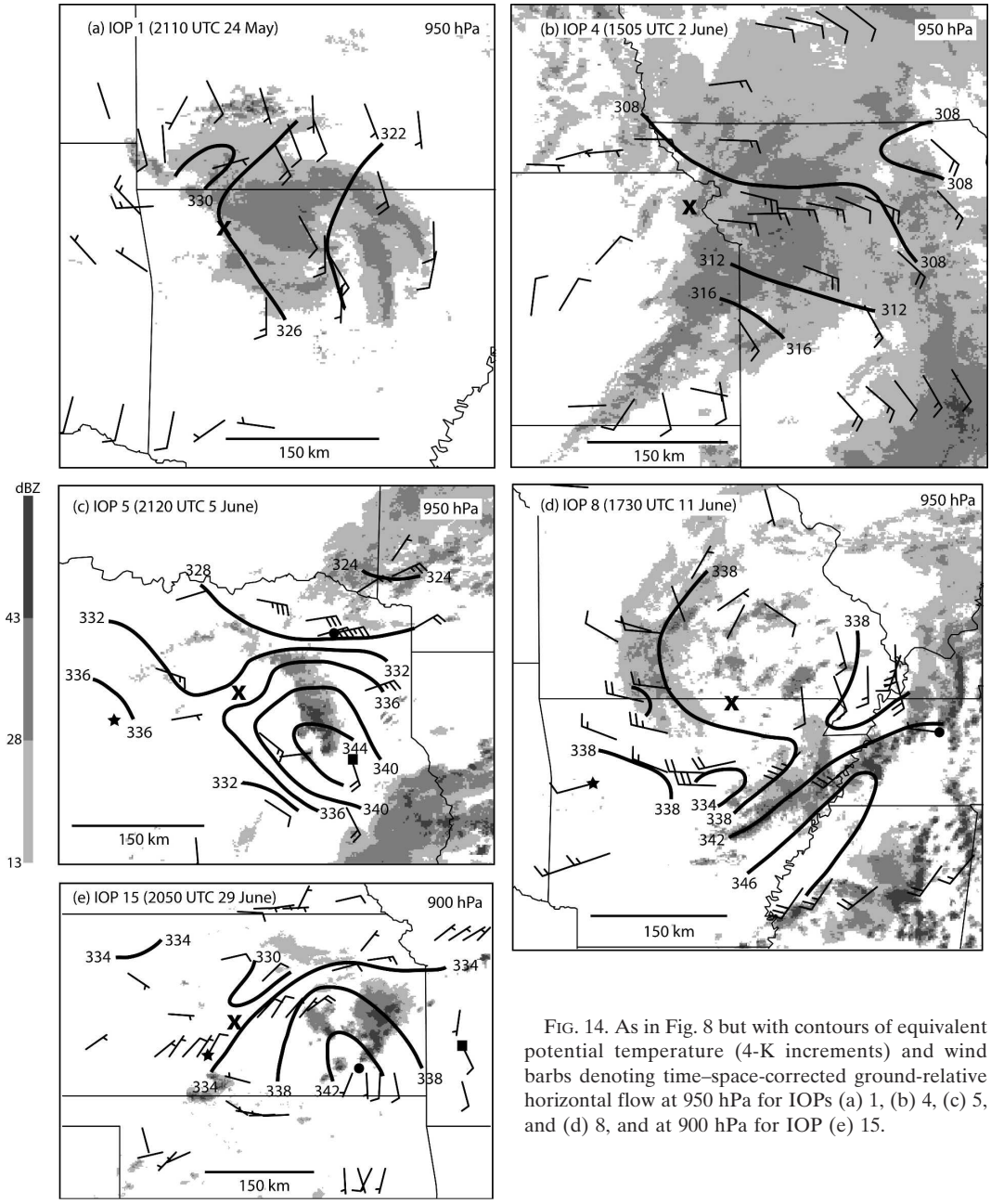


FIG. 14. As in Fig. 8 but with contours of equivalent potential temperature (4-K increments) and wind barbs denoting time–space-corrected ground-relative horizontal flow at 950 hPa for IOPs (a) 1, (b) 4, (c) 5, and (d) 8, and at 900 hPa for IOP (e) 15.

capped by a significant 850-hPa dry inversion, which inhibits even shallow cumulus (square in Fig. 16a). However, along the southeastern (downshear) periphery of the MCV, a dropsonde deployed only 16 min later in the vicinity of the organizing deep convection (Fig. 16a, circle) reveals cooler conditions above the PBL from ~900 to 700 hPa (solid black in Fig. 16b) than farther east (solid gray in Fig. 16b), consistent with the downshear lower-tropospheric mesoscale ascent occurring above the PBL (Figs. 8e, 9f). Also important to convection initiation in this case is the considerably greater PBL moisture (dashed black in Fig. 16b), consistent with the localization of high $\theta_e$ air along the downshear periphery of the MCV (Fig. 14e).

An upshear dropsonde deployed at 1959 UTC (star in Fig. 16a) slightly downstream from the $\theta_e$ minimum on the west side of the PBL circulation in IOP 15 (Fig. 14e) exhibits significantly reduced PBL moisture relative to downshear (dashed curves in Fig. 16c) but, in contrast to IOP 5 (solid curves in Fig. 15c), does not

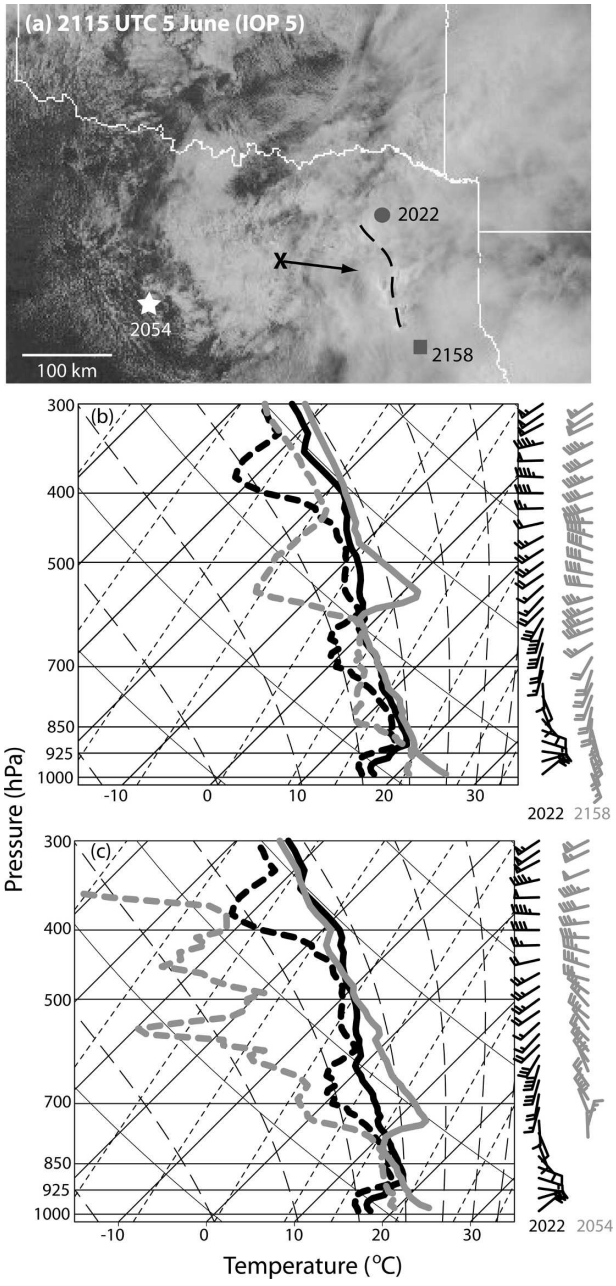


FIG. 15. (a) Visible satellite imagery for IOP 5 with the location of the 600-hPa MCV center indicated by the "x" and the magnitude and orientation of the 900–600-hPa environmental vertical shear vector (Table 2) indicated by the arrow. The dashed line highlights the location of the developing convective line depicted in Fig. 4a and referred to in the text. (b), (c) Temperature (boldface solid lines) and dewpoint (boldface dashed lines) curves and ground-relative wind profiles (wind barb symbols at right) for the dropsonde times and the non-time–space-corrected locations annotated in (a). In (b) black plots are for 2022 UTC and gray plots for 2158 UTC. In (c) black plots are for 2022 UTC and gray plots for 2054 UTC.

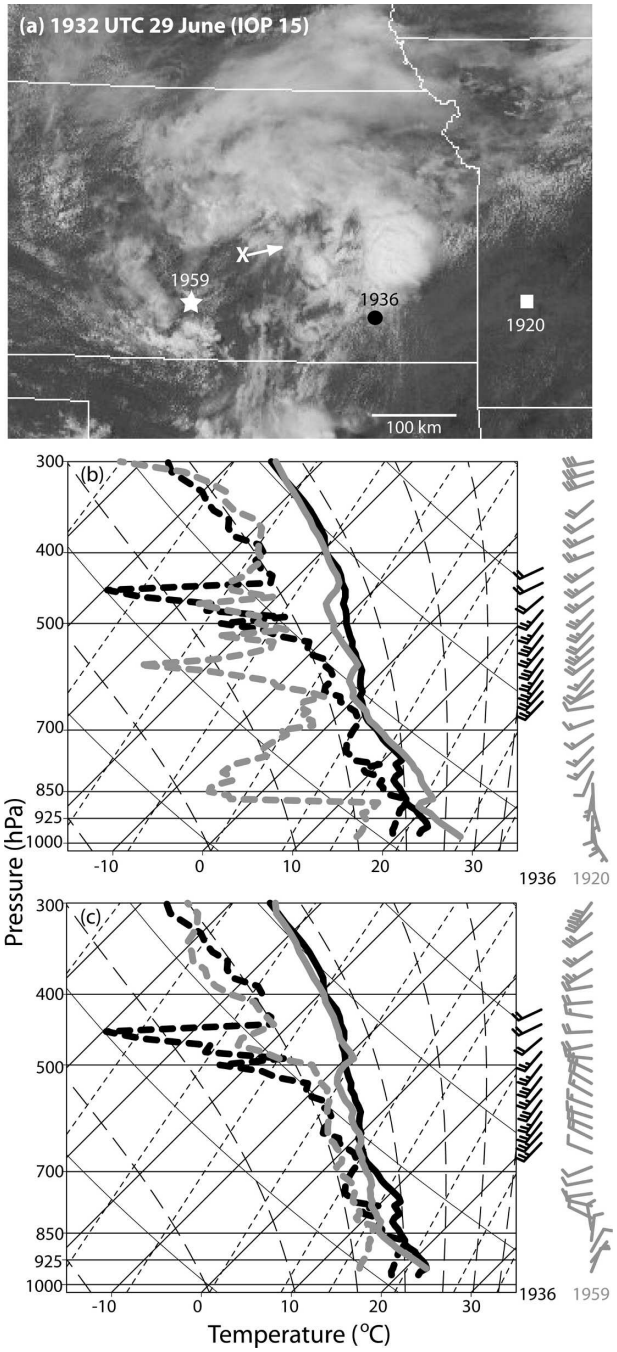


FIG. 16. As in Fig. 15 but for IOP 15. In (b) black plots are for 1936 UTC and gray plots for 1920 UTC. In (c) black plots are for 1936 UTC and gray plots for 1959 UTC.

show any warming above the PBL relative to downshear (solid curves in Fig. 16c) and also lacks a subsidence inversion. Clearly, horizontal advections within the PBL play a major role in the thermodynamic stability in the vicinity of the MCV in IOP 15, where mesoscale vertical motions are weaker than in IOP 5.

### 3) IOP 8

Despite similar bulk thermodynamic properties in the downshear and upshear regions for IOP 8 (Figs. 10e, 11e), an examination of dropsondes separated by the approximate diameter of the MCV circulation reveals considerable variability (Fig. 17). Similar to the weaker MCV in IOP 15, advection of high-$\theta_e$ air in the PBL is conducive to convection initiation along the southeast periphery of the MCV (Fig. 14d). In IOP 8, however, the larger and much stronger midtropospheric vortex clearly penetrates to the surface (Part I, their Fig. 6d). Here, a dropsonde deployed at 1757 UTC in advance of a developing band of convection (circle in Fig. 17a) is influenced at the lowest levels by cool outflow but exhibits a moist, conditionally unstable layer from 925 to 850 hPa (black curves in Fig. 17b) with little convective inhibition (CIN).

Similar to IOP 5 (gray curves in Fig. 15c), a dropsonde deployed 41 min later upshear, southwest of the MCV center (star in Fig. 17a), exhibits a strong, dry inversion above a well-mixed PBL (gray curves in Fig. 17b). The dry inversion results in a deep layer of CIN that conditionally unstable air parcels originating in the PBL along the southwest periphery of the MCV (Fig. 13d) are unable to overcome. Although the lower-tropospheric dry inversion is located in weak 800-hPa kinematic ascent (Figs. 8d, 12d), it is downstream from kinematic descent (Figs. 8d, 12d) and expansive isentropic descent (Fig. 12i) associated with the mesoscale cold advection pattern in this part of the vortex (Part I, their Fig. 5d). Thus, assuming steady conditions, the lower-tropospheric vertical motions in Figs. 8d, 12d,i are consistent with prior descent occurring for air that composes the dry inversion layer.

### 4) SYNTHESIS OF CASES

The foregoing analysis of the three secondary convection cases indicates large variation of lower–midtropospheric thermodynamic vertical structure and conditional instability across the MCV circulations. The sense of the thermodynamic variations is consistent with differences in the lower–midtropospheric vertical motion and lower-tropospheric horizontal temperature and moisture advections across the vortices. However, it is unlikely that their magnitude can be entirely explained by MCV-induced motions in all cases. For instance, the large differences in lower-tropospheric moisture between the downshear part of the MCV and its downstream environment in IOP 15 (Fig. 16b) are also influenced by large-scale variability that precedes the MCV. It was noted earlier that the mesoscale vertical motions are particularly strong in the nearly stationary IOP 5 MCV (Figs. 8c, 9d). However, even in this case, the MCV circulation alone may not entirely account for the excessively dry midtropospheric conditions on the upshear side of the MCV (Figs. 15c). Here, previous drying associated with the descending rear inflow (not shown) of the large antecedent MCS (Part I, their Fig. 3c) that dissipated earlier in this region could also be influential. Although they do not act alone, the MCV-induced motions *systematically* contribute to thermodynamic destabilization downshear and thermodynamic stabilization upshear and, thus, clearly provide a focus for secondary convection. That the locations where secondary convection occurred for all three cases are similar relative to the MCV centers further supports the notion that the MCVs favorably influenced its development.

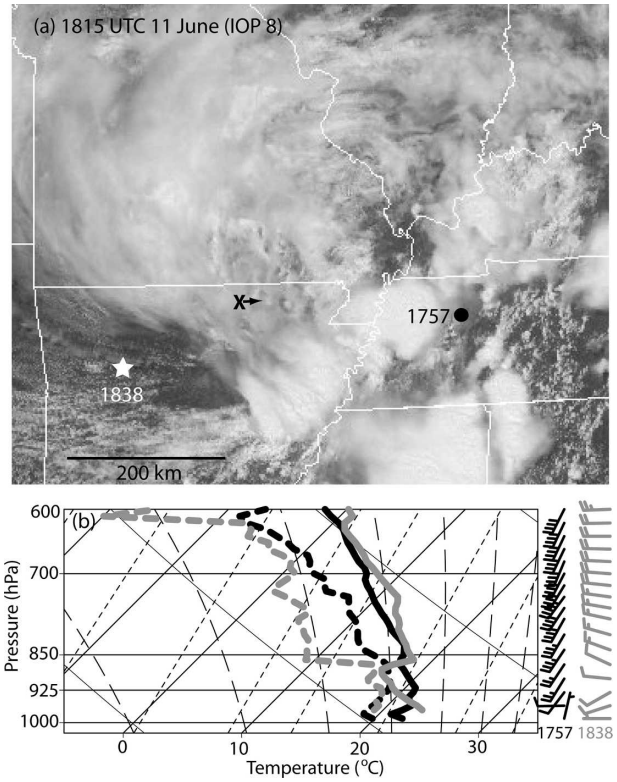


FIG. 17. As in Fig. 15 but for IOP 8. In (b) black plots are for 1757 UTC and gray plots for 1838 UTC.

### c. *Vertical shear across the MCV*

MCV-related modifications to the vertical shear result from a variety of factors including vortex tilt and differences in vortex intensity with height. These modifications can increase or decrease the local magnitude of the vertical shear depending on how the MCV-induced part superposes on the environmental vertical

shear (e.g., Knievel and Johnson 2002). This in turn can influence the strength and organization of deep convection.

Since the MCVs are most intense in the midtroposphere and occur in westerly environmental vertical shear (Part I), the enhancement of the zonal component of the lower-tropospheric vertical shear to the right (approximately south) of the environmental vertical shear vector occurs for each of the IOPs except IOP 5 (Fig. 18a). The anomalous stronger vertical shear in the sector to the left of the environmental vertical shear vector in IOP 5 is consistent with the most intense part of the east–west-oriented lower-tropospheric baroclinic zone occurring north of the MCV center (Part I, their Fig. 5c). From thermal wind considerations, this could account for the enhanced westerly shear north of the MCV center, which fully counteracts the MCV-induced shear modifications. This effect could also influence the *u*-component vertical shear in IOP4 (Part I, their Fig. 5b) but is apparently not strong enough to fully counteract the MCV-induced shear (Fig. 18a).

Meridional components of vertical shear increase from the upshear to downshear sectors by ~5–15 m $s^{-1}$ depending on the IOP (Fig. 18b). This is consistent with the southerly vortex tangential flow increasing with height downshear and, similarly, northerlies increasing with height on the upshear side of the MCV. Systematic but typically weaker (0–6 m $s^{-1}$) zonal vertical shear increases from the upshear to downshear sector (Fig. 18b) also occur and are consistent, from thermal wind considerations, with the greater intensity of the east–west-oriented lower-tropospheric frontal zone downshear of the MCV center (Part I, their Fig. 5). Average vertical shear magnitudes within different MCV quadrants (Table 5) are greater than environmental estimates (section 3) in all but the UL quadrant.[4] The largest average increase is 4 m $s^{-1}$ in the DR quadrant, although large variations among the cases occur.

Increases in vertical shear magnitude over those of the environment are consistent with the development of at least moderately strong linearly organized convection in the downshear quadrants for cases with conditional instability (IOPs 5, 8, and 15). The possibility that these shear increases are influenced by the deep convection itself cannot be dismissed. However, convection is relatively localized at the time of sampling in most cases and there is no evidence of *widespread* low-$\theta_e$ convectively induced outflows in any of the cases (Fig. 14). This suggests that these regional differences in the vertical shear result primarily from the MCV circulation.

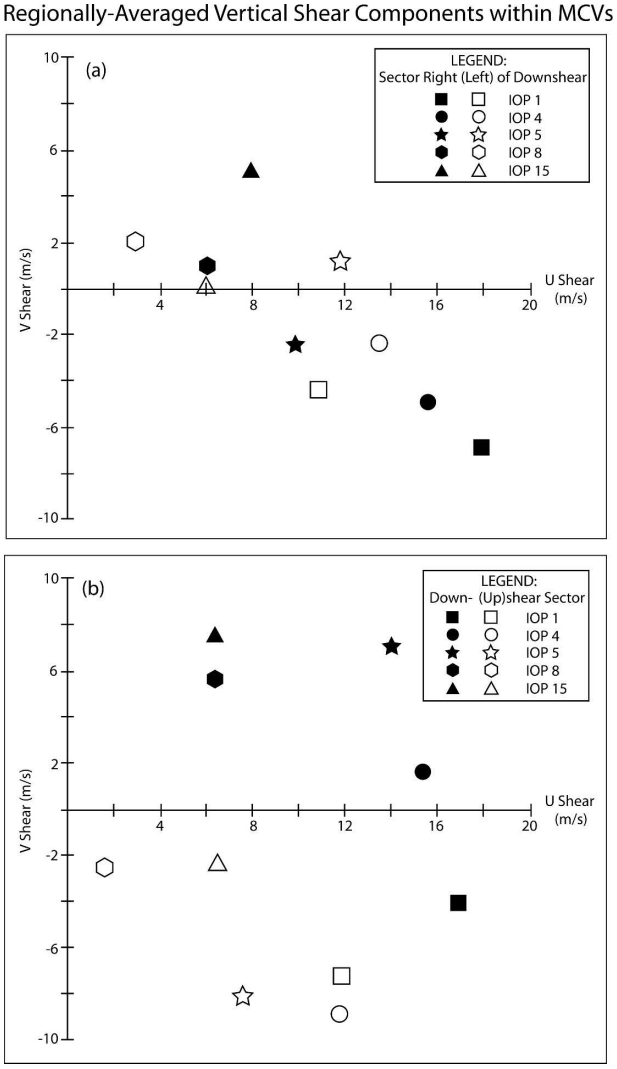


FIG. 18. Average zonal and meridional components of the vertical difference in horizontal winds between 350 hPa above the surface pressure and an average of the lowest 100 hPa AGL within 180° sectors (a) both to the right (filled symbols) and left (open symbols) of the environmental vertical shear vector and (b) downshear (filled symbols) and upshear (open symbols) of the environmental vertical shear vector.

## 6. Summary and discussion

In the present study, we have examined the occurrence of daytime precipitation in five mature long-lived MCVs sampled during the Bow Echo and MCV Experiment (BAMEX). Although details of the precipi-

[4] The estimates of magnitude are based on vector averages of gridded data from the quadrants, which slightly underrepresent the average local magnitudes (parenthetical values in Table 3) because of variability in vertical shear direction within the quadrants.

TABLE 5. Magnitudes (m s$^{-1}$) of vectors constructed from gridded quadrant-averaged (from 0.5 to 1.5 times the RMWs) zonal and meridional components (Fig. 18) of the horizontal wind difference from 350 hPa above the surface pressure and an average for the lowest 100 hPa AGL. The location of the quadrants relative to the environmental vertical shear vector for the example IOP 4 case is illustrated in Fig. 7a. Values in parentheses represent quadrant-averaged magnitudes of the same vertical differences of horizontal winds. The environmental condition is determined from an average of all quadrants using gridded data from the MCV center to a radial distance of 1.5 times the RMWs.

| Location | IOP 1 | IOP 4 | IOP 5 | IOP 8 | IOP 15 | Average |
|---|---|---|---|---|---|---|
| DL | 14.6 (14.9) | 14.0 (16.0) | 17.4 (18.3) | 10.7 (11.3) | 6.9 (8.1) | 12.7 (13.8) |
| DR | 20.2 (21.2) | 17.3 (18.0) | 14.2 (15.6) | 6.3 (7.6) | 13.0 (13.4) | 14.2 (15.1) |
| UL | 9.5 (10.5) | 16.1 (16.5) | 11.5 (12.7) | 3.7 (6.4) | 6.5 (7.3) | 9.5 (10.7) |
| UR | 18.4 (18.6) | 13.5 (13.7) | 11.0 (13.2) | 6.2 (7.8) | 8.1 (8.7) | 11.4 (12.4) |
| Environment | 13.4 | 16.0 | 12.1 | 4.1 | 5.5 | 10.2 |

tation organization varied widely among cases, the heaviest precipitation typically occurred from near the center of the MCV to its downshear periphery, while upshear quadrants remained relatively precipitation free.

The availability of detailed horizontal wind and thermodynamic field data enabled the diagnosis of the lower–midtropospheric vertical motions within the downshear and upshear regions of the MCV, which constitutes a novel aspect of this study. Vertical motion patterns within the MCV circulation for the five cases appear influenced by the ratios of the strengths of environmental vertical shear and the vortex strength.

For $\Delta U/V_R > 1$ (IOPs 5 and 15), where $\Delta U$ is the environmental vertical shear magnitude through the depth of the vortex (Part I, their Fig. 8) and $V_R$ is the maximum vortex tangential flow (Part I, their Table 1), a well-defined vertical motion dipole existed at levels below those of the vortex center. Here, although amplitudes were significantly greater than those associated with the vortex-relative isentropic component alone, the kinematically derived vertical motion pattern strongly resembled this conceptual model (Fig. 1), which includes lower-tropospheric isentropic ascent downshear and isentropic descent upshear of the MCV circulation center.

For the only strong MCV in weak environmental vertical shear $\Delta U/V_R < 1$ (IOP 8), the vertical motion pattern was considerably more complicated and did not appear to be systematically related to environmental vertical shear. Two other cases (IOPs 1 and 4) exhibited broad regions of ascent, which were strongest downshear of the MCV center. However, in these cases, it is more difficult to conclude the significance of the vortex–environmental shear interaction mechanism in influencing mesoscale lifting since widespread precipitation occurred across much of the MCV circulation at the time of analysis (particularly downshear).

Significant secondary convection developed within the MCV circulation in three of the five IOPs and its location was spatially correlated with locations of the greatest conditional instability located downshear of the MCV circulation center. The MCVs that persisted for a significant time in conditionally stable environments (IOPs 1 and 4) were associated with widespread heavy stratiform precipitation and thus also have implications for quantitative precipitation forecasting.

The conditional instability in the secondary convection cases was governed to first order by the synoptic thermodynamic conditions but was modified substantially across the MCV. We were unable to follow the evolution of the MCV circulation and related changes in the thermodynamic structure using our time–space-composited dataset. However, comparisons of the vertical structure of temperature and moisture in dropsondes from the downshear and upshear regions of the MCV circulation were consistent with idealized modeling studies (e.g., Trier et al. 2000b) that illustrate how MCVs predispose mesoscale regions to secondary convection.

In particular, the mesoscale ascent within these MCVs contributed to thermodynamic destabilization by cooling and moistening the lower- and midtropospheric layers above the PBL downshear from the vortex center, which favored secondary convection. Similarly, mesoscale subsidence warmed and dried lower- and midtropospheric layers above the PBL on the upshear side of the MCVs, which inhibited secondary convection. The thermodynamic vertical structure was influenced by other factors including lower-tropospheric temperature and moisture advections and differential surface heating, which varied significantly across the MCVs. Since MCVs extend downward into the lower troposphere, where temperature and moisture increase from north to south, horizontal advections significantly enhanced conditional instability on the east side, while decreasing it on the west side of the MCV in several of the cases.

The vertical shear was significantly modified within the MCV, with the largest increases in vertical shear

magnitude occurring, on average, along and to the right of the lower-tropospheric (~950–650 hPa) environmental vertical shear vector. However, which MCV sectors had the most vertical shear varied among individual cases. This uncertainty is influenced by a variety of factors including differences in the structure of the vortex (including tilt and asymmetries), environmental features (including fronts), and the spatial relationships among them. Thus, being able to forecast how MCV-induced vertical shear will *locally* influence deep convection within any given case remains a formidable challenge. Despite this uncertainty, we found that on average, the vertical shear was enhanced above environmental values within three of the four MCV quadrants (Table 5), which indicates that MCVs can provide an environment conducive to severe convective weather given sufficient conditional instability.

This study has emphasized the influence of MCVs on the mesoscale environment of convection. Overall, the quadrant to the right of the environmental vertical shear vector (e.g., DR quadrant in Fig. 7a) was found to be the most supportive of secondary convection, consistent with its being the location of greatest average mesoscale vertical motions, conditional instability, and vertical shear within the MCV circulation. However, further study is required to understand the finescale details that govern exactly how secondary convection was initiated. We also emphasize that the response of the thermodynamic vertical structure to the MCV-induced motions and their interaction with other environmental factors portrayed in this study may only be strictly applicable to daytime situations. Nocturnal convection that occurs within some of the longest-lived MCVs (e.g., Wetzel et al. 1983; Fritsch et al. 1994; Trier and Davis 2002) may be influenced by different combinations of environmental and MCV-related factors.

*Acknowledgments.* The authors thank the BAMEX dropsonde coordinators, David Ahijevych, George Bryan, and Jason Knievel (each of NCAR), Diana Bartels (NOAA/Forecast Systems Laboratory), Richard James (the Pennsylvania State University), Dan Hawblitzel (Texas A&M University), and Susan van den Heever (Colorado State University), whose outstanding efforts were critical to the collection of the unprecedented dataset used in this study. We also acknowledge the skillful operation of the Lear jet by Weather Modification Incorporated and many of the staff from the former Atmospheric Technology Division (now Earth Observing Laboratory) of NCAR who were responsible for MGLASS and dropsonde operation. We further thank David Ahijevych for providing scripts that we modified to run the GEMPAK software used to plot data, and Jason Knievel is acknowledged for a helpful internal review of a draft of this manuscript. We acknowledge the constructive comments of Richard Moore (ETH Zürich) and two anonymous reviewers, and thank Stephan Nelson (NSF) for his support of the BAMEX Lear jet operations.

## REFERENCES

Bartels, D. L., and R. A. Maddox, 1991: Midlevel cyclonic vortices generated by mesoscale convective systems. *Mon. Wea. Rev.,* **119,** 104–118.

Bellamy, J. C., 1949: Objective calculations of divergence, vertical velocity and vorticity. *Bull. Amer. Meteor. Soc.,* **30,** 45–49.

Benjamin, S. G., and Coauthors, 2004: An hourly assimilation–forecast cycle: The RUC. *Mon. Wea. Rev.,* **132,** 495–518.

Bosart, L. F., and F. Sanders, 1981: The Johnstown flood of July 1977: A long-lived convective system. *J. Atmos. Sci.,* **38,** 1616–1642.

Brandes, E. A., 1990: Evolution and structure of the 6–7 May 1985 mesoscale convective system and associated vortex. *Mon. Wea. Rev.,* **118,** 109–127; Corrigendum, **118,** 990.

Carbone, R. E., J. W. Conway, N. A. Crook, and M. W. Moncrieff, 1990: The generation and propagation of a nocturnal squall line. Part I: Observations and implications for mesoscale predictability. *Mon. Wea. Rev.,* **118,** 26–49.

Davies-Jones, R., 1993: Useful formulas for computing divergence, vorticity, and their errors from three or more stations. *Mon. Wea. Rev.,* **121,** 713–725.

Davis, C. A., and S. B. Trier, 2002: Cloud-resolving simulations of mesoscale vortex intensification and its effect on a serial mesoscale convective system. *Mon. Wea. Rev.,* **130,** 2839–2858.

——, and ——, 2007: Mesoscale convective vortices observed during BAMEX. Part I: Kinematic and thermodynamic structure. *Mon. Wea. Rev.,* **135,** 2029–2049.

——, D. A. Ahijevych, and S. B. Trier, 2002: Detection and prediction of warm season midtropospheric vortices by the Rapid Update Cycle. *Mon. Wea. Rev.,* **130,** 24–42.

——, and Coauthors, 2004: The Bow Echo and MCV Experiment: Observations and opportunities. *Bull. Amer. Meteor. Soc.,* **85,** 1075–1093.

Frank, W. M., and E. A. Ritchie, 1999: Effects of environmental flow upon tropical cyclone structure. *Mon. Wea. Rev.,* **127,** 2044–2061.

Fritsch, J. M., J. D. Murphy, and J. S. Kain, 1994: Warm core vortex amplification over land. *J. Atmos. Sci.,* **51,** 1780–1807.

Jiang, H., and D. J. Raymond, 1995: Simulation of a mature mesoscale convective system using a nonlinear balance model. *J. Atmos. Sci.,* **52,** 161–174.

Johnston, E. C., 1981: Mesoscale vorticity centers induced by mesoscale convective complexes. M.S. thesis, Dept. of Meteorology, University of Wisconsin—Milwaukee, 54 pp.

Jorgensen, D. P., and B. F. Smull, 1993: Mesovortex circulations seen by airborne Doppler radar within a bow-echo mesoscale convective system. *Bull. Amer. Meteor. Soc.,* **74,** 2146–2157.

Knievel, J. C., and R. H. Johnson, 2002: The kinematics of a midlatitude, continental mesoscale convective system and its mesoscale vortex. *Mon. Wea. Rev.,* **130,** 1749–1770.

Leary, C. A., and E. N. Rappaport, 1987: The lifecycle and internal structure of a mesoscale convective complex. *Mon. Wea. Rev.,* **115,** 1503–1527.

Menard, R. D., and J. M. Fritsch, 1989: A mesoscale convective complex-generated inertially stable warm core vortex. *Mon. Wea. Rev.,* **117,** 1237–1261.

O'Brien, J. J., 1970: Alternative solutions to the classical vertical velocity problem. *J. Appl. Meteor.,* **9,** 197–203.

Raymond, D. J., 1992: Nonlinear balance and potential-vorticity thinking at large Rossby number. *Quart. J. Roy. Meteor. Soc.,* **118,** 987–1015.

——, and H. Jiang, 1990: A theory for long-lived mesoscale convective systems. *J. Atmos. Sci.,* **47,** 3067–3077.

Rogers, R. F., and J. M. Fritsch, 2001: Surface cyclogenesis from convectively driven amplification of midlevel mesoscale convective vortices. *Mon. Wea. Rev.,* **129,** 605–637.

Spencer, P. L., and C. A. Doswell III, 2001: A quantitative comparison between traditional and line integral methods of derivative estimation. *Mon. Wea. Rev.,* **129,** 2538–2554.

——, P. R. Janish, and C. A. Doswell III, 1999: A four-dimensional objective analysis scheme and multitriangle technique for wind profiler data. *Mon. Wea. Rev.,* **127,** 279–291.

Trier, S. B., and C. A. Davis, 2002: Influence of balanced motions on heavy precipitation within a long-lived convectively generated vortex. *Mon. Wea. Rev.,* **130,** 877–899.

——, ——, and J. D. Tuttle, 2000a: Long-lived mesoconvective vortices and their environment. Part I: Observations from the central United States during the 1998 warm season. *Mon. Wea. Rev.,* **128,** 3376–3395.

——, ——, and W. C. Skamarock, 2000b: Long-lived mesoconvective vortices and their environment. Part II: Induced thermodynamic destabilization in idealized simulations. *Mon. Wea. Rev.,* **128,** 3396–3412.

Wetzel, P. J., W. R. Cotton, and R. L. McAnelly, 1983: A long-lived mesoscale convective complex. Part II: Evolution and structure of the mature complex. *Mon. Wea. Rev.,* **111,** 1919–1937.